Contents lists available at ScienceDirect

Applied Catalysis B: Environmental

Ethanol conversion at low temperature over CeO$_2$—Supported Ni-based catalysts. Effect of Pt addition to Ni catalyst

Tamara Siqueira Moraes [a,b], Raimundo Crisostomo Rabelo Neto [a], Mauro Celso Ribeiro [a,1], Lisiane Veiga Mattos [b], Marios Kourtelesis [c], Spyros Ladas [c], Xenophon Verykios [c], Fábio B. Noronha [a,*]

[a] Instituto Nacional de Tecnologia, Av. Venezuela 82, Rio de Janeiro 20081-312, Brazil
[b] Universidade Federal Fluminense, Rua Passo da Pátria, 156, Niterói 24210-240, Brazil
[c] Department of Chemical Engineering, University of Patras, 26504 Patras, Greece

ABSTRACT

The effect of Pt addition on the performance of Ni/CeO$_2$ catalyst for the low temperature steam reforming of ethanol is investigated. The reaction mechanism was explored using diffuse reflectance infrared spectroscopy under reaction conditions and temperature-programmed surface reaction of ethanol. The addition of Pt to Ni/CeO$_2$ catalyst promoted the decomposition of dehydrogenated and acetate species to hydrogen, methane, CO and carbonate species. Furthermore, the presence of Pt reduced the rate of catalyst deactivation. In situ X-ray absorption studies revealed the formation of a nickel carbide phase during steam reforming of ethanol over Ni/CeO$_2$ catalyst, which was associated with amorphous carbon deposition and catalyst deactivation. X-ray photoelectron spectroscopy in combination with kinetic and structural data was consistent with a partial Pt monolayer on Ni in the bimetallic catalyst. The segregation of Pt on the surface of the Ni particles minimized the formation of nickel carbide and promoted catalyst stability.

© 2015 Elsevier B.V. All rights reserved.

1. Introduction

Hydrogen production through steam reforming (SR) of ethanol has been extensively studied in the literature [1–7]. Coke formation is a major issue in SR of ethanol, which may lead to a decrease in catalytic activity and selectivity toward hydrogen and to catalyst deactivation. Carbon formation may take place via several reactions, such as ethanol dehydration to ethylene, followed by polymerization to coke; the "Boudouard" reaction; the decomposition of hydrocarbons (methane and ethylene) [5,6]. The extent of each reaction depends on both catalyst used and reaction conditions.

Carbon deposition may be avoided at high operating temperatures (above 700 °C), where high hydrogen yield can be also achieved [5]. However, high reaction temperatures enhance the formation of byproduct CO, due to the thermodynamically favored reverse water gas shift (RWGS) reaction. For PEM fuel cell applications, the concentration of CO should be less than 10 ppm, as dictated by the poisoning limit of Pt electrodes [8]. To achieve this limit, complex further treatment of reformate gas is required [9–11].

Low temperature steam reforming (LTSR) of ethanol is a very attractive approach for suppressing carbon deposition. In this case, ethanol may undergo decomposition, yielding a mixture of H$_2$, CH$_4$ and carbon oxides. In addition, the water gas-shift (WGS) reaction is favored in this temperature range, contributing to the reduction of CO concentration. However, the development of suitable catalysts which are able to produce a H$_2$ rich stream with very low CO concentration is still a challenge. Such a stream could be used directly in fuel cells producing power.

Several catalysts based on Ni, Co, Cu, Ir, Pt, Rh, Pd and Ru dispersed on different supports (e.g., Al$_2$O$_3$, CeO$_2$, La$_2$O$_3$, ZrO$_2$, Y$_2$O$_3$, ZnO, Sm$_2$O$_3$, TiO$_2$, V$_2$O$_5$ and MgO) have been studied for the LTSR [12–23]. Generally, supported Pt catalysts exhibit higher activity and selectivity and therefore are more widely studied. The superior performance of Pt over Rh, Ru and Pd was shown in our previous study [12]. In spite of their lower cost, supported non-noble metal catalysts are less studied for the LTSR of ethanol. Zhang et al. [16] studied the SR of ethanol over Ir, Ni and Co supported on ceria. They

found that the reaction pathways of LTSR of ethanol depended on the ability of the metals for the C—C bond breaking. Over Ir/CeO_2 catalyst, dehydrogenation of ethanol to acetaldehyde was the main reaction, whereas ethanol decomposition to methane and CO was promoted over Ni/CeO_2 catalyst. The activity and H_2 selectivity varies in the order of Ir > Ni > Co over CeO_2-supported catalysts. The superior performance of Ir was assigned to the intimate contact between Ir particles and ceria, as well as to the ceria-mediated redox process, which greatly enhances both ethanol reforming and WGS reactions. Therefore, the support plays a key role in the LTSR of ethanol. Bimetallic catalysts have been less investigated for LTSR [18,19,24–31] and the numbers of papers about PtNi catalysts is scarce [18,19,31–33]. Palma et al. [32,33] reported that $NiPt/CeO_2$ catalyst prepared by first addition of Ni to ceria followed by impregnation of Pt revealed a higher activity and selectivity. However, carbon formation was observed. Palma et al. [18] also developed a kinetic model for the LTSR of ethanol (613–753 K) over a $PtNi/CeO_2$ catalyst. However, carbon deposition was still observed at 723 K on the bimetallic catalyst. Sanchez-Sanchez et al.[19] investigated the mechanism of SR of ethanol at 673 K over $PtNi/Al_2O_3$ catalyst. The authors proposed that the improved stability of the bimetallic catalyst is due to a cooperative effect between Pt and Ni that promotes the gasification of the methyl groups formed as a result of the decomposition of the acetate species. However, the bimetallic particles were not characterized in order to explain the origin of this cooperative effect.

The effect of the nature of the support for the LTSR of ethanol has been investigated over a variety of metal catalysts supported on oxide and mixed oxide supports. It has been found that the WGS activity of dispersed platinum strongly depends on the physico-chemical characteristics of the support [11,34,35]. The beneficial effect of CeO_2 for the LTSR of ethanol has been reported by Ciambelli et al. [36], who found a higher hydrogen yield for Pt/CeO_2 than for Pt/Al_2O_3 catalyst. Product distribution was also found to be influenced by the nature of the support, with Pt/CeO_2 catalyst exhibiting higher selectivities toward H_2 and CO_2 and lower selectivity toward CO, due to the enhancement of the WGS reaction. The ethanol decomposition was favored over Pt/Al_2O_3 catalyst, leading to higher selectivities toward CH_4 and CO. The improved catalytic performance of Pt/CeO_2 is related to the greater ability of CeO_2 to release and store oxygen, resulting in higher stability compared to Pt/Al_2O_3 [13].

In addition to carbon deposition, the oxidation of the metal particles during SR of ethanol may also contribute to catalyst deactivation [37,38]. Temperature-programmed X-ray absorption near edge structure (XANES) experiments of Co/CeO_2-Al_2O_3 and Co-Pt/CeO_2-Al_2O_3 under SR and OSR of ethanol revealed strong oxidation of cobalt particles [37]. The oxidation of metallic cobalt occurred mainly within the temperature range of 573–673 K, which are typical temperatures of LTSR of ethanol.

Aim of this work is to investigate the performance of Ni, Pt and PtNi catalysts supported on CeO_2 for LTSR of ethanol. In the present paper we report on the structural and catalytic effects of addition of Pt to Ni catalysts supported on CeO_2. Several *in situ* techniques (DRIFTS, TPSR of ethanol, XPS and XAFS) were used in order to investigated whether the NiPt alloy was formed or not and to follow possible alterations in catalyst structure under reaction conditions.

2. Experimental

2.1. Catalyst preparation

CeO_2 was prepared by addition of an aqueous solution of $Ce(NO_3)_3 \cdot 6H_2O$ to a NaOH solution ($C_{NaOH} = 6$ mol/L). After precipitation, the material was dried at 383 K and calcined at 773 K for 5 h

in air flow. Ni/CeO_2 and Pt/CeO_2 catalysts were prepared by incipient wetness impregnation of the support with aqueous solutions of $Ni(NO_3)_3 \cdot 6H_2O$ or H_2PtCl_6 in order to obtain 10 wt.% of Ni and 1 wt.% of Pt, respectively. After impregnation, the sample was calcined at 673 K for 4 h in air flow. $PtNi/CeO_2$ catalyst containing 10 wt.% Ni and 1 wt.% Pt was synthesized by co-impregnation of the support, using aqueous solution of $Ni(NO_3) \cdot 6H_2O$ and H_2PtCl_6. Then, the sample was treated under the same conditions as previously described.

2.2. Catalyst characterization

The chemical composition of each sample was determined with a Wavelength Dispersive X-ray Fluorescence Spectrometer (WD-XRF S8 Tiger, Bruker) with a rhodium tube operated at 4 kW. The analyses were performed with the samples (300 mg) in powder form using a semi-quantitative method (QUANT-EXPRES/Bruker).

The BET surface areas of the samples were measured using a Micromeritics ASAP 2020 analyzer with nitrogen adsorption at liquid nitrogen temperature.

Catalysts were also characterized in terms of their dispersion and mean crystallite size by dual CO chemisorption at 298 K and the experimental procedure is described in the supplementary information. The CO hydrogenation reaction was carried out at 823 K over Pt/CeO_2 catalyst before and after SR of ethanol reaction to estimate possible changes in Pt dispersion during the SR reaction. Two experiments were performed. In the first one, the sample (100 mg) was reduced under the same conditions used for SR of ethanol. Then, the reactant mixture (30 mL/min H_2 and 10 mL/min CO) was passed through the catalyst. In the second experiment, SR of ethanol was performed at 773 K for 28 h TOS. Then, the reaction was stopped by cutting the ethanol flow. The catalyst was heated to 823 K and the CO hydrogenation reaction was carried out.

TPR experiments were performed in a TPR/TPD 2900 Micromeritics system equipped with a thermal conductivity detector (TCD). The catalyst was pretreated at 473 K for 1 h under a flow of air prior to the TPR experiment The reducing mixture (5.0% H_2/N_2) was passed through the sample (100 mg) at a flow rate of 30 mL/min and the temperature was increased to 1273 K at a heating rate of 10 K/min.

Conventional *ex-situ* XPS measurements in a MAX200 (LEYBOLD/SPECS) Electron Spectrometer using non-monochromatic MgKα radiation (1253.6 eV) and an EA200-MCD analyzer operated at a constant pass energy (PE) of 100 eV were carried out along the surface normal on samples prepared as described above (Section 2.1), then reduced in flowing hydrogen and stored under atmospheric conditions. The binding energy (BE) scale was corrected for electrostatic charging by setting at 284.8 eV the main C1s peak due to atmospheric specimen surface contamination. The uncertainty in the corrected BE values due to random measurement errors is of the order of ±0.15 eV. The relative sensitivity factor (RSF) database used for quantitative analysis has been adapted to the MAX200 spectrometer operating conditions from the empirical collection of Wagner et al. as described elsewhere [39].

In situ photoelectron spectroscopy measurements were carried out immediately following specimen reduction, using tunable synchrotron radiation at the Brazilian Synchrotron Light Source, with the soft X-rays beamline equipped with a spherical grating monochromator (SGM), in the 100–1000 eV energy range. The incident photon energy was adjusted for each spectrum so that the peak(s) of interest would appear with the same kinetic energy around 620 eV, using the PHOIBOS HSA3500 analyzer operated at a PE of 30 eV and the same slit aperture for all spectra. The analysis was performed at 45° with respect to the surface normal and the peak areas for quantitative analysis were normalized with respect to the measured incident beam intensity. The relative sensitivity factors (RSF) for each photopeak do not depend on

the analyzer transmission characteristics and the thickness of any surface contamination layer and thus have been based on relative atomic shell cross-sections and asymmetry factors adapted to the sample-analyzer geometry [40].

Thermogravimetric analysis of the used catalysts was carried out in a TA Instruments equipment (SDT Q600) in order to determine the amount of carbon formed over the catalyst. Approximately 10 mg of spent catalyst was heated under air flow from room temperature to 1273 K at a heating rate of 20 K/min and the weight change was measured.

SEM analyses of the spent catalysts were carried out using a field emission scanning electron microscope (FE-SEM) Quanta FEG 450 FEI operating with an accelerating voltage of 20 kV.

Raman was used to characterize the nature of carbon formed on the catalysts after 28 h TOS. The Raman spectra were recorded using a Horiba LabRam HR-UV800/Jobin-Yvon Spectrometer, equipped with He-Ne laser ($\lambda = 632$ nm) with 10 mW of intensity, a CCD detector and an Olympus BX41 microscope with objective lens of $100\times$.

In-situ XAS experiments were performed at the D04B-XAFS—1 beamline of the Brazilian Synchrotron Light Source (LNLS, Campinas). Typically, wafers containing pressed mixtures of the sample with BN as a binder were then placed into a sample holder located inside a quartz tubular reactor. EXAFS spectra at the Ni K edge ($E_0 = 8.333$ keV) were successively recorded, while the sample underwent the following treatment: (i) heating ramp under a 5% H_2/He mixture at 10 K min^{-1} up to 773 K, (ii) temperature hold for 1 h at 773 K, (iii) sample cooling down to 573 K, under a 5% H_2/He mixture flow, (iv) flowing mixture shift to a reactant mixture containing 98% He, 1.5% H_2O, 0.5% ethanol for 2 h (SR of ethanol conditions), (v) sample cooling down to room temperature under He flow. Data treatment was made using the ATHENA software package [41]. The composition of metallic Ni phase during sample activation (reduction under H_2/He flow) was monitored by linear combination of normalized Ni K-edge XANES spectra (LC-XANES) within the 8.3-8.43 keV energy range, using Ni foil and NiO as references for Ni^0 and Ni^{2+}, respectively.

In order to investigate the occurrence of a PtNi solid solution after pretreatment of the samples, Pt L$_{III}$ -edge spectra were recorded in the fluorescence mode in the XAFS-2 beamline at the LNLS. In those experiments, the samples were packed into a 1.0 (I.D.) x1.2 (O.D.) mm capillary reactor, placed inside a furnace, whose temperature was controlled via a thermocouple placed inside the reactor, close to the catalyst bed. The reactor was then placed at 45^0 degrees relative to the beam, while a Camberra Ge 15 channel solid state detector was placed at a normal angle relative to the beam to collect the fluorescence signal. The procedure in this study is similar to the one formerly described, with the difference that all spectra were recorded at room temperature, to minimize thermal effects in the measurements.

2.3. Mechanistic studies

Temperature-programmed surface reaction (TPSR) experiments were carried out employing the apparatus and procedure described in detail elsewhere [42,43]. In a typical TPSR experiment, the catalysts (100 mg) were reduced *in situ* at different temperatures (at 573 K for Pt/CeO$_2$, at 773 K for PtNi/CeO$_2$, and Ni/CeO$_2$) under H_2 flow (30 cm^3/min) for 30 min. The sample was then heated under He flow (30 cm^3/min) at 773 K for 15 min to remove adsorbed species from the catalyst surface and subsequently cooled to room temperature. At this point the feed composition was switched to a mixture containing 0.5% CH$_3$CH$_2$OH + 1.5% H$_2$O (in He) (30 cm^3 min^{-1}). The temperature was then increased linearly ($\beta = 15$ K/min) up to 1023 K.

An Omnistar/Pfeiffer Vacuum mass spectrometer (MS) was used for on-line monitoring of effluent gas composition. The transient-MS signals at $m/z = 2$ (H$_2$), 15 (CH$_4$), 18 (H$_2$O), 28 (CO), 44 (CO$_2$), 31 (C$_2$H$_5$OH), 29 (C$_2$H$_4$O), 26 (C$_2$H$_4$), 27 (C$_2$H$_6$), 39 (C$_3$H$_6$) and 59 (C$_4$H$_{10}$O) were continuously recorded. Responses of the mass spectrometer were calibrated against standard mixtures of accurately known composition.

Fourier transform infrared (FTIR) experiments were carried out using a Nicolet 6700 apparatus equipped with a diffuse reflectance (DRIFT) cell (Spectra Tech), an MCT detector and a KBr beam splitter. In a typical experiment, the catalyst powder was heated at 723 K under He flow for 10 min and then reduced in flowing hydrogen (20% H$_2$ in He) at 573 K for Pt/CeO$_2$, and at 773 K for PtNi/CeO$_2$ and Ni/CeO$_2$ catalysts, for 60 min. The cell was then flushed with He at 723 K for 10 min and subsequently cooled down to room temperature (RT) under He flow. During the cooling stage, background spectra were collected at temperatures of interest. The flow over the pretreated sample was then switched to a gas mixture consisting of 0.5% EtOH and 1.5% H$_2$O, at RT for 15 min. Temperature was increased in a stepwise mode up to 723 K and spectra were obtained at selected temperatures after equilibration for 15 min-on-stream. After recording the spectrum, temperature was increased to the next selected temperature. To investigate the deactivation of the catalyst, several spectra were recorded during steady-state SR reaction at 573 K over 6 h.

2.4. Kinetic measurements

SR of ethanol was performed in a fixed-bed reactor at 573 K and atmospheric pressure. Prior to reaction, samples (100 mg) were reduced under pure hydrogen (30 mL/min) at 773 K for 1 h and then purged under N$_2$ at the same temperature for 30 min. The reactant mixture (2.5% ethanol; 7.5% water, 90.0% nitrogen) was obtained by flowing two N$_2$ streams (30 mL/min) through each saturator containing ethanol and water separately, which were maintained at the temperature required to obtain the desired H$_2$O/ethanol molar ratio of 3.0. The reaction products were analyzed by gas chromatography (Micro GC Agilent 3000 A) containing three channels for three thermal conductivity detectors (TCD) and three columns: a molecular sieve, a Poraplot Q and OV-1. Ethanol conversion and selectivity to various products were determined as previously described [4].
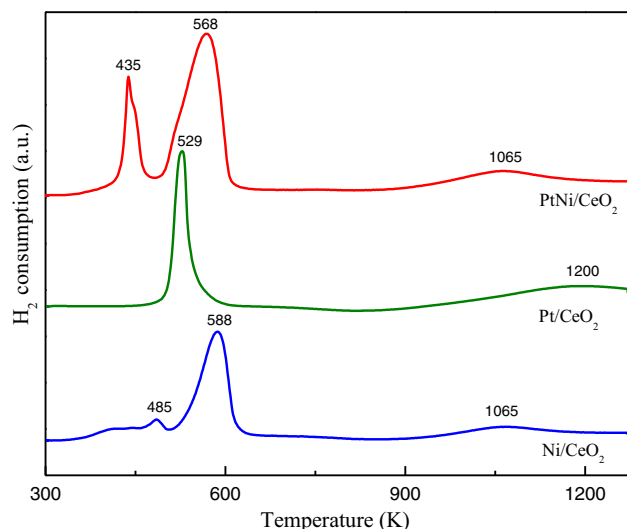
Specific reaction rate measurements were also carried out. In a typical experiment, 20 mg of fresh catalyst was placed in a fixed-bed reactor and reduced *in situ* at 573 K for Pt/CeO$_2$, and at 773 K for PtNi/CeO$_2$ and Ni/CeO$_2$ catalysts, for 90 min, under a hydrogen flow of 40cc/min. The ethanol/water mixture is pumped into a vaporizer maintained at 503 K and mixed with the gas stream coming from the mass-flow controllers. The resulting gas mixture is then fed into the reactor through stainless steel tubing maintained at 433 K. The reaction products were analyzed by two gas chromatographs connected in parallel through a common set of switch valves. The first GC is equipped with two packed columns (Porapak-Q, Carbosieve) and two detectors (TCD, FID) and operates with He as the carrier gas. The second GC is equipped with a Carbosieve column and a TCD detector. This chromatograph uses N$_2$ as the carrier gas and is solely used for the determination of H$_2$ in the reformate gas.

Measurements of intrinsic reaction rates were obtained in experiments with varying flow rates (200–450 cm^3/min) and reaction temperature (573–700 K). In all experiments, conversion of ethanol was kept below 10% so that differential reaction conditions could be assumed. When experimental conditions were changed, the catalyst sample was exposed to air for 30 min., followed by reduction in hydrogen flow for 90 min. Temperature experiments were conducted in both ascending and descending order. Values of specific rates, along with measurements of metal dispersion (Table 1), were used to calculate turnover frequencies (TOF), which

Table 1
BET surface area, chemical composition, metal dispersion and metal particle size of the catalysts.

Sample	Surface area (m^2/g)	Chemical composition		(%)	Metal dispersion (%)	Metal particle size (nm)
		Pt	Ni	CeO_2		
CeO_2	91	–	–	–	–	–
Pt/CeO_2	118	1.0	–	98.9	58	2
Ni/CeO_2	79	–	9.3	88.5	9	12
PtNi/CeO_2	81	1.1	10.8	84.7	7	15

Fig. 1. TPR profiles of CeO_2, Ni/CeO_2, Pt/CeO_2 and PtNi/CeO_2.

is defined as moles of ethanol converted per surface metal atom per second. In all experiments, the reaction was conducted under negligible external and internal heat and mass transfer limitation, as estimated theoretically, applying various criteria.

3. Results and discussion

3.1. Catalyst characterization

The BET surface area of the CeO_2 support was 91 m^2/g. The impregnation of Ni and the co-impregnation of Ni and Pt did not significantly affect the surface area of the catalysts. On the other hand, the addition of Pt led to an increase of surface area (Table 1). The chemical composition of the samples was close to the nominal values (Table 1). Furthermore, traces of chlorine and sodium were not detected by FRX and XPS techniques. Table 1 also lists the metal dispersion of all catalysts. Pt/CeO_2 catalyst showed the highest metal dispersion (58%), whereas Ni-based catalysts have approximately the same value (7 and 9%).

For Pt/CeO_2 catalyst, a sharp peak at 529 K and broad hydrogen consumption at 1200 K are observed (Fig. 1). The peak at 529 K can be attributed to the reduction of PtO_2. However, the H_2 consumption of this first peak (0.69 mol H_2/mg$_{cat}$) (Table 2) is larger than the theoretical H_2 consumption of PtO_2 (0.09 mol H_2/mg$_{cat}$). Therefore, this result shows that the H_2 uptake at 529 K cannot be attributed only to the reduction of PtO_2. The first peak corresponds not only to PtO_2 reduction but also to CeO_2 surface reduction [44]. The metal can facilitate the reduction of the surface shell of ceria from Ce^{4+} to Ce^{3+} by H_2 dissociation and spillover. The peak at 1200 K is ascribed to bulk CeO_2 reduction.

The TPR profile of Ni/CeO_2 catalyst exhibited three peaks at 485, 588 K and 1065 K. Hydrogen consumption in the first peak was attributed to the decomposition of residual nickel nitrates [45]. Hydrogen uptake in the second peak was higher than that necessary for complete reduction of NiO (Table 2). This result indicates that reduction of NiO to Ni^0 occurs along with the reduction of surface ceria, which is promoted by the presence of metallic nickel. The broad reduction peak at high temperature could also comprise the reduction of bulk ceria.

For the bimetallic catalyst, in addition to the peaks at 568 and 1065 K, there is also a peak at 435 K. This peak is partly attributed to the reduction of PtO_2. However, the H_2 consumption of the first peak (0.52 mol H_2/mg$_{cat}$) was much higher than the theoretical H_2 consumption of PtO_2 (0.09 mol H_2/mg$_{cat}$). This excess of H_2 consumption could be attributed to the promoted reduction of CeO_2 support (as observed for Pt/CeO_2 catalyst) and/or of NiO by the metallic platinum particles. In fact, the H_2 uptake of the second peak (1.57 mol H_2/mg$_{cat}$) was lower than the theoretical H_2 consumption necessary for the complete reduction of NiO (1.70 mol H_2/mg$_{cat}$). This result suggests that part of NiO was reduced in the first peak and indicates that Pt and Ni are in close contact in the bimetallic catalyst. The peak at 1065 K is likely due to the formation of Ce_2O_3.

Ex-situ XPS resulted in the expected detection of Ce, Ni, O and C in Ni-based catalysts studied, whereas Pt was detected only in the bimetallic catalyst. Carbon from atmospheric surface contamination was found in both specimens, whereas the average level of other surface impurities, like Na^+, within the analyzed region was below the detection limit of the measurement that is less than ~0.7 at.% with respect to Ce. Fig. S1 shows the Ni2p–Ce3d spectral region, which is similar for both samples. The Ce 3d region exhibits the expected characteristic multiplet structure for CeO_2 with a strong satellite at 916.4 eV BE corresponding to Ce(IV) [46]. The Ni $2p_{3/2}$ peak appears as a broad region between 855 and 853 eV BE arising from a mixture of NiO and Ni^0 features, as a result of superficial oxidation of the Ni nanoparticles upon exposure to the atmosphere. The Pt 4f region is superimposed on the broad Ni3p spectrum (Fig. S2) with at $4f_{7/2}$ at 72.1 eV, which is about 1 eV higher than that expected for bulk metallic Pt. Alloying of Pt within the Ni particles is not supported, since in 1:1 Pt-Ni bulk alloys, a small lowering of the BE for Pt $4f_{7/2}$ by ~0.35 eV has been observed [47]. As the TPR results indicate close proximity between Ni and Pt, the high Pt$4f7/2$ BE could be more likely due to a differential charging due to the presence of non conductive oxidized nickel on the bimetallic particle surface and/or to very slight oxidation, given that the Pt$4f_{7/2}$ BE for PtO and PtO_2 is 74.0 and 74.9 eV, respectively. In the *in-situ* photoemission measurements there is a large uncertainty in measured BE because of the weaker signal and the difficulty in electrostatic charging correction. The Ni3p broad spectrum which had to be used, due to experimental limitations at the synchrotron, is not as sensitive to chemical state as Ni2p, but its peak maximum at ~67 eV is within experimental uncertainty consistent with metallic Ni. The BE of Pt$4f7/2$ at 70.9 ± 0.3 eV definitely suggests metallic Pt, but cannot exclude alloying. However evidence against alloying is given from the quantitative analysis of the *in situ* data in the following paragraph.

Quantification of the XPS results was based on measured peak area ratios and the respective relative sensitivity factors (RSF), whereby Ce3d, Ni2p$_{3/2}$, Pt4f were used in the *ex-situ* and Ce4d, Ni3p, Pt4f in the *in-situ* measurements. The average metal-to-Ce

Table 2
Hydrogen consumption from TPR profiles.

Sample	First peak (mol H$_2$/mg$_{cat}$)[a]	Second peak (mol H$_2$/mg$_{cat}$)[b]	Third peak (mol H$_2$/mg$_{CeO2}$)[c]
Pt/CeO$_2$	0.69	–	0.43
Ni/CeO$_2$	–	2.08	0.81
PtNi/CeO$_2$	0.52	1.57	0.38

[a] Theoretical H$_2$ consumption of PtO$_2$ = 0.09 mol H$_2$/mg$_{cat}$.
[b] Theoretical H$_2$ consumption of NiO = 1.70 mol H$_2$/mg$_{cat}$.
[c] Theoretical H$_2$ consumption of CeO$_2$ = 2.61 mol H$_2$/mg$_{CeO2}$.

Table 3
Summary of quantitative XPS results

Sample	Measured metal-to-Ce average atomic ratio	Simulated parameters for a model of 'disk-shaped' 'Ni' particles (fractional support coverage, θ_{Ni}, average height, H$_{Ni}$), without (Ni-only) or with (Pt-Ni) a partial monolayer of Pt with coverage θ_{Pt} on top		
		$\theta_{Ni/CeO2}$	H$_{Ni}$ (nm)	$\theta_{Pt/Ni}$ (h$_{Pt}$~0.27nm)
Ni/CeO$_2$-ppt				
Ex-situ	0.357	0.123	1.35 (Ni^0 +NiO)	---
In-situ	0.316	0.115	1.30 (Ni^0)	---
PtNi/CeO$_2$-ppt				
Ex-situ	0.914 (Ni)	0.317	0.68 (Ni^0 +NiO)	0.10
In-situ	0.023 (Pt)			
	0.389 (Ni)	0.151	1.2 (Ni^0)	0.15
	0.028 (Pt)			

atomic ratios in the analyzed region (assuming a non-realistic uniform atomic distribution) are first shown in Table 3. The more realistic way the metallic phase is dispersed on ceria was then probed by simulating the above ratios [39], assuming island-like arrays of disk-shaped particles (Ni, Pt or PtNi), each with average height H and arbitrary diameter D covering a fraction Θ of the available support surface area. Further simulation details are presented in the Supplementary Information. The simultaneous estimation of H and Θ was achieved under two conditions: (1) That the calculated Ni(2p$_{3/2}$ or 3p)/Ce(3d or 4d) and Pt4f/Ce(3d or 4d) peak intensity ratios reproduce the corresponding experimental ratios; (2) That the number of Ni or Pt atoms in the array per unit ceria surface area be consistent with the measured metal loading of the samples distributed equally over the entire measured support BET surface area. Alternative Pt-Ni relative arrangement models were also tested for the bimetallic sample. Given that a close proximity between Pt and Ni exists, as indicated by other observations in this work, a model whereby Pt forms an atomic overlayer covering 10–15% of the Ni particles surface, in contrast to full intra-particle alloying, is the only one fully consistent, even within a considerable experimental uncertainty, with the XPS data, both *ex-situ* and *in-situ*. The main source of uncertainty in distinguishing among the various relative arrangements of Pt and Ni in the mixed nanoparticles is the uncertainty in the experimental intensity ratios which had to be simulated (condition 1 above). This uncertainty is estimated at ~10% for the ex-situ data and ~30% for the in-situ data, due to the weaker signal in the latter case. The corresponding simulation results are also shown in Table 3. In any case, the average disk-shaped Ni particle height is of the order of 1 nm, however the average particle diameter that would be needed in order to estimate dispersion cannot be obtained directly from the XPS data. It should be pointed out that although the Pt-Ni bulk phase diagram might favor Pt-Ni intermixing, one may claim that nano- or sub-nano-metric particles do not always behave properly in that respect. Given the small value of the nominal Pt/Ni atomic ratio (~0.03) very small Ni particles might contain only a few Pt atoms therefore intermetallics with high Pt content are likely not relevant and the segregation energetics could be different than bulk predictions based on the bulk phase-diagram. One could also point out that the Pt overlayer model as obtained by the simulation of the XPS data cannot be practically distinguished from a Pt-Ni surface alloy within the outermost atomic layer of the bimetallic particle.

3.2. Mechanistic aspects of the LTSR of ethanol reaction

Mechanistic aspects of the ethanol steam reforming reaction have been investigated with the use of transient – MS and FTIR techniques. The TPSR profile obtained over the 10% Ni/CeO$_2$ catalyst is shown in Fig. 2A. Ethanol is observed in the gas phase at temperatures as high as 530 K. In the same region, the appearance of a broad and weak peak corresponding to acetaldehyde desorption is observed. At 350 K, the ethanol dehydrogenation reaction (CH$_3$CH$_2$OH $\leftrightarrows$ CH$_3$CHO + H$_2$) is initiated with hydrogen being the main product detected in the gas phase. Acetaldehyde probably remains mainly adsorbed on the catalyst surface. At 450 K, the signal of ethanol in the gas phase start to decrease while the CO, CH$_4$ and H$_2$ concentrations increase, indicating that ethanol decomposition (CH$_3$CH$_2$OH → CH$_4$ + H$_2$ + CO) occurs. However, the concentration of hydrogen is significantly higher than that of CO and CH$_4$, indicating the occurrence of ethanol dehydrogenation. The concentrations of CO and CH$_4$ are similar and smaller than that of hydrogen, indicating that ethanol dehydrogenation is followed by acetaldehyde decomposition (CH$_3$CHO → CH$_4$ + CO). Apparently, ethanol dehydrogenation is faster than acetaldehyde decomposition and mostly acetaldehyde remains on the surface until higher temperatures are achieved, when its decomposition is favorable.

In the temperature range of 523–623 K, an increase in the concentrations of CO$_2$ and H$_2$, following the same slope, is observed. This clearly indicates the occurrence of the WGS reaction (CO + H$_2$O $\leftrightarrows$ CO$_2$ + H$_2$). However, the concentration of CO increases slightly in this temperature range. This can be explained by considering simultaneous decomposition reactions and the WGS reaction. Thus, CO participates in the WGS as reactant and as product in ethanol and/or acetaldehyde decomposition. Above 600 K, there is a concomitant reduction of CO and H$_2$ concentrations, whereas the signal of methane still increases. This is due to the occurrence of the methanation reaction (CO + 3H$_2$ $\leftrightarrows$ CH$_4$ + H$_2$O).

The dominant reactions at temperatures above 750 K seem to be the reverse WGS, as well as dry reforming of methane (CH$_4$ + CO$_2$ $\leftrightarrows$ 2CO + 2H$_2$) and steam reforming of methane (CH$_4$ + H$_2$O $\leftrightarrows$ CO + 3H$_2$) and ethanol (CH$_3$CH$_2$OH + 2H$_2$O $\leftrightarrows$ 2CO + 4H$_2$)
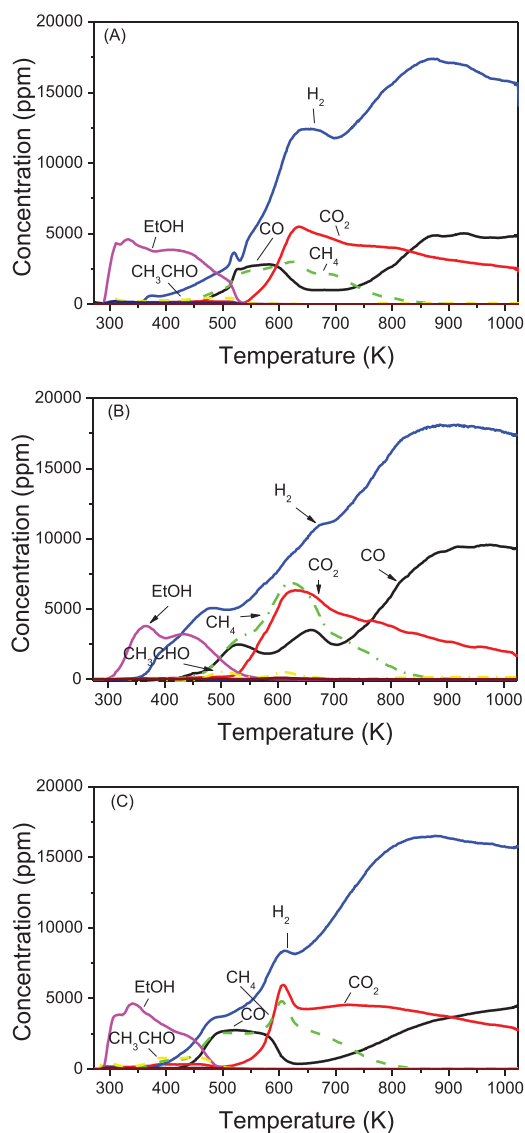
Fig. 2. TPSR spectra under ethanol steam reforming conditions over (A) Ni/CeO$_2$; (B) Pt/CeO$_2$; (C) PtNi/CeO$_2$.

resulting in higher hydrogen and CO concentrations, and lower CO$_2$ concentrations.

For Pt/CeO$_2$ catalyst (Fig. 2B), the TPSR profile does not seem to be significantly different than that of the Ni catalyst. A small increase in catalytic activity over the Pt catalyst is manifested in a shift of certain product signals towards lower temperatures. Ethanol dehydrogenation reaction is initiated at about 350 K as well, but H$_2$ concentration is higher than that over the Ni catalyst. This result suggests that the amount of acetaldehyde formed is higher on Pt than on Ni-based catalyst. In fact, the presence of two desorption peaks of acetaldehyde at 500 and 600 K is observed. Acetaldehyde and/or ethanol decomposition begins at lower temperature (420 K), as observed by the variation of CO, CH$_4$ and H$_2$ signals. At 520 K, the significant increase of CO$_2$ and H$_2$ concentration suggests the occurrence of the WGS at a rather high rate. Qualitatively, exactly the same reactions seem to take place, as in the case of the Ni/CeO$_2$ catalyst, but activity is shifted toward lower temperatures. In addition to this difference, the methane concentration profile seems to differ significantly. A close inspection of the CH$_4$ profiles of Fig. 2A and B shows that it consists of two peaks, at about 500 K and 600 K. The first peak is attributed primarily to acetaldehyde decomposition. The acetaldehyde decomposition

route involves the decomposition of acetate species formed, as demonstrated by DRIFTS results, which will be presented in a subsequent section. The second peak, however, is much higher over the Pt/CeO$_2$ as compared to Ni/CeO$_2$ catalyst. As stated earlier, this second peak is attributed mainly to CO methanation. The higher intensity of the second methane peak of Pt/CeO$_2$ catalyst in comparison to Ni/CeO$_2$ catalyst implies that the former catalyst is more active than the later in CO hydrogenation. It is generally accepted that Ni is more active in CO hydrogenation than Pt, probably due to the lower CO dissociation energy on Pt [48]. In the present case, however, CeO$_2$ could be playing a significant role in this reaction route by supplying spillover oxygen species on the metal surface which could influence catalytic activity significantly. In the case of Pt, this phenomenon would be much more pronounced due to the higher dispersion of Pt on CeO$_2$, compared to Ni on CeO$_2$ (Table 1). The higher intensity of the second methanation peak on the profile of Pt/CeO$_2$ could be also due to the higher decomposition rate of acetaldehyde to CO, the reactant of the methanation reaction.

Addition of Pt to the Ni/CeO$_2$ catalyst does not seem to cause significant differences in the reaction scheme, as evidenced by the spectra presented in Fig. 2C. The same reactions that take place over the Ni/CeO$_2$ catalyst can be observed in the bimetallic catalyst. This agrees very well with kinetic results, which will be presented in a subsequent section. In particular, ethanol dehydrogenation is initiated at 373 K, and acetaldehyde decompositions at a slightly lower temperature, as witnessed by the H$_2$, CO and CH$_4$ responses. The occurrence of the WGS reaction above 500 K is apparent from the variation of H$_2$ and CO$_2$ concentrations. A second methane peak at 620 K is clearly observed, as for the Pt-based catalyst, indicating that CO methanation is taking place at a very high rate over this catalyst. This might be due to the presence of Pt atoms on the surface of Ni crystallites, as suggested by the XPS experiments, and also due to an enhancement of CO hydrogenation activity of Ni in the presence of Pt atoms [49,50]. The enhancement of the CO methanation activity of Ni may be due to spillover of adsorbed hydrogen atoms from Pt to neighboring Ni atoms.

It must be noted at this point that the first methane peak (at about 500 K), which is attributed to acetaldehyde decomposition, does not seem to be affected by the presence of Pt on the catalyst surface, in contrast to the second peak (at about 620 K) which is significantly affected, as discussed above.

The *in situ* DRIFT spectra obtained following exposure of the Ni/CeO$_2$ catalyst to a 0.5% ethanol and 1.5% water (balance He) mixture at 298K for 30 min and subsequent stepwise heating up to 723K, under continuous flow of the reaction mixture, are shown in Fig. 3A. It is observed that the spectrum recorded at 298 K (trace a) is dominated by bands corresponding to different vibrational modes of ethoxy species formed by dissociative adsorption of ethanol over Ce cations (2974, 2884, 1377, 1099 and 1057 cm^{-1}) [51–55]. The peaks located at 2974 and 2884 cm^{-1} can be attributed to asymmetric C—H stretching vibrations in methyl groups ($\nu_{as}(CH_3)$) and symmetric C—H vibrations in methylene groups ($\nu_s(CH_2)$), respectively [54]. It is observed that ethanol adsorption leads to the formation of monodentate and bidentate ethoxy species identified by the CH$_3$ bending (1377 cm^{-1}: $\delta(CH_3)$) and CO stretching (1099, 1057 cm^{-1}: $\nu(C-O)$) vibrations. The band located at 1643 cm^{-1} is probably related to the $\nu(CO)$ vibrational mode of either adsorbed acetyl or acetaldehyde species [5]. These species can be produced by dehydrogenation of a fraction of the ethoxy species towards acetaldehyde, which may be further dehydrogenated to acetyl species [5]. The bands at 1425 cm^{-1} and 1557 cm^{-1} [51,52,54] to correspond to symmetric OCO and asymmetric OCO stretching modes of acetate species.

Stepwise increase of temperature from 298 to 473 K (traces b–d) results in a decrease in intensities of ethoxy species which are present in the spectra up to 573 K, whereas the band attributed
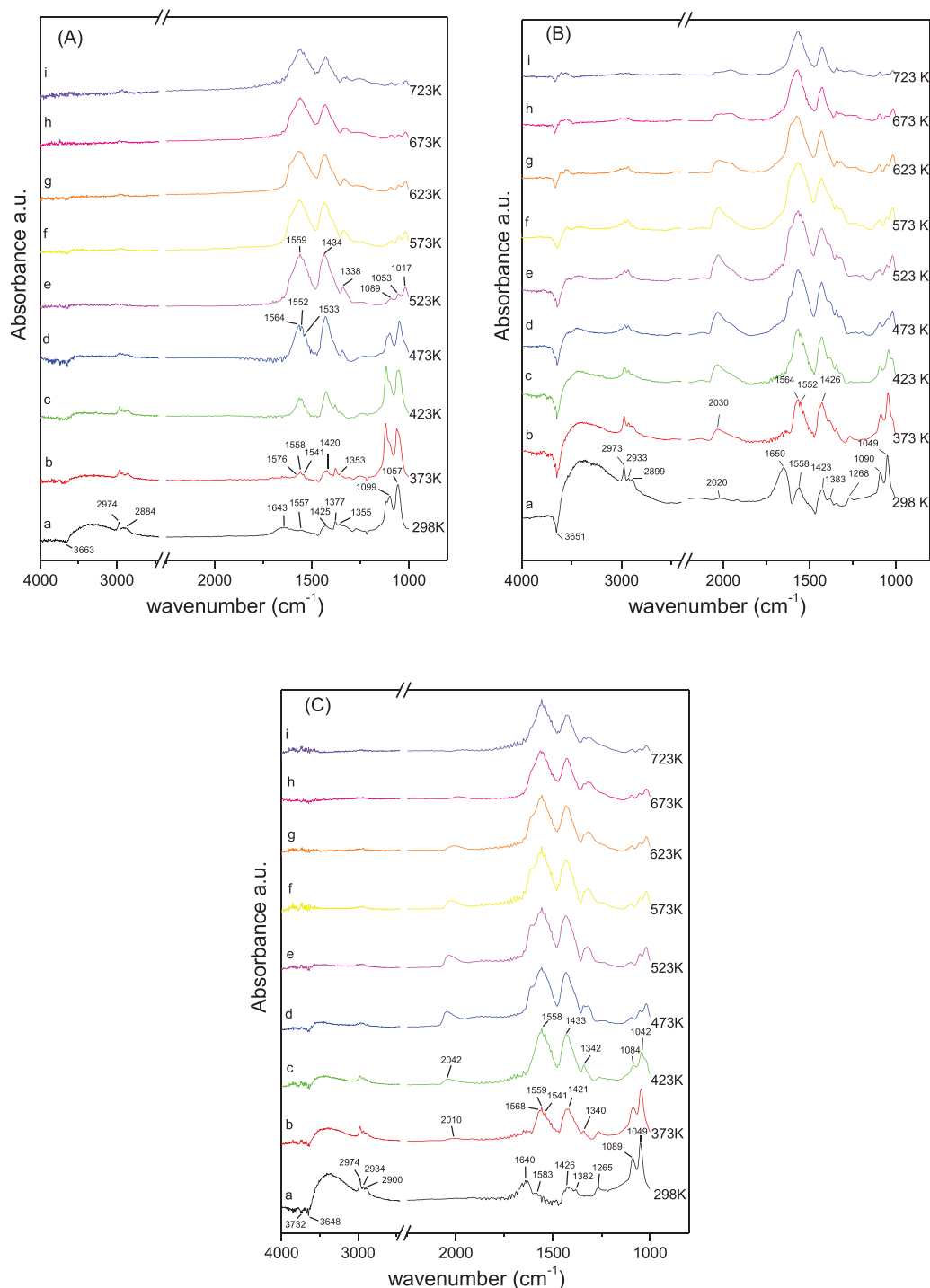
Fig. 3. DRIFT spectra obtained over (A) Ni/CeO$_2$; (B) Pt/CeO$_2$ and (C) PtNi/CeO$_2$ catalyst, under the reaction mixture 0.5% ethanol, 1.5% water (He balance) and stepwise heating at 723 K under continuous flow.

to acetyl species disappeared by the temperature of 373 K. On the other hand, the intensity of the bands related to acetate species significantly increased. These results indicate that ethoxy species are oxidized to acetate species. As discussed above, it has been proposed that ethoxy species are dehydrogenated to acetaldehyde, which may in turn be further dehydrogenated to acetyl species. Acetate species can be formed either by interaction of acetaldehyde with surface OH groups and/or reaction between the acetyl species and oxygen originating from the support [53,56,57]. The presence of acetate species has been previously attributed to the large avail-

ability of oxygen from the ceria support [52]. However, the bands at 2884 and 2974 cm^{-1} were no longer observed after heating at 473 K. Therefore, it can be assumed that the acetate species were oxidized to carbonate species. According to the literature [5], the acetate species can either decompose to form CH$_4$ and CO or further oxidize to produce carbonate species, which in turn may dissociate to give CO$_2$. At higher temperatures, the relative intensities of the bands related to acetate or carbonate species were observed to form broad bands at the same wavenumbers.

Similar FTIR spectra were obtained when the same experiment was conducted over the Pt/CeO$_2$ catalyst (Fig. 3B). The spectrum exhibits the bands corresponding to different vibrational modes of ethoxy species (2973, 2933, 2899, 1383, 1090 and 1049 cm^{-1}). The band at 1268 cm^{-1}, has been assigned to ethanol molecularly adsorbed on the Lewis acid sites of the oxide [58]. Moreover, a band at 1643 cm^{-1} is probably related to the ν(CO) vibrational mode of adsorbed acetyl species, whereas those at 1558 and 1423 cm^{-1}, to acetate species. However, a new band at 2020 cm^{-1} can be discerned, which can be attributed to the ν(CO) vibrational mode of linearly adsorbed CO on metal particles [59]. This result suggests that ethanol was decomposed to CH$_4$, H$_2$ and CO even at room temperature.

Increasing temperature from 298 to 523 K results in a decrease in the relative intensities of the bands attributed to ethoxy species, whereas the band attributed to acetyl species completely disappeared. On the other hand, the intensity of the bands related to acetate species and linearly adsorbed CO significantly increased. Further increase of temperature reduced the intensity of the bands assigned to acetate species and adsorbed CO. However, the bands at 2933 and 2973 cm^{-1} were no longer observed after heating at 673 K, probably due to the oxidation of acetate to carbonate species.

Comparison of the spectra obtained over Ni/CeO$_2$ and over Pt/CeO$_2$ catalysts reveals that Ni favors the formation of carbonate species, whereas Pt promotes more effectively ethanol decomposition to CH$_4$, H$_2$ and CO, even at room temperature. The presence of the negative bands associated with surface OH groups over the Pt/CeO$_2$ catalyst up to 723 K is a further indication that carbonate formation by oxidation of acetate species takes place to a much lower extent than over Ni catalyst.

DRIFT spectra under ethanol–water mixture for PtNi/CeO$_2$ catalyst are presented in Fig. 3C. The same characteristic bands are observed, including bands of ethoxy species (2974, 2934, 2900, 1382, 1089 and 1049 cm^{-1}), acetyl species (1640 cm^{-1}) and acetate species (1426 and 1583 cm^{-1}). When the sample was heated to 373 K, the bands characteristic of ethoxy and acetyl species disappeared. The intensities of the bands assigned to acetate species increased and a new band appeared in the spectra at 2010 cm^{-1}, which can be attributed to the ν(CO) vibrational mode of linearly adsorbed CO on metal particles [59]. Increasing temperature to 523 K increased the intensity of the band of the linearly adsorbed CO on Pt. However, the bands corresponding to C—H stretching modes of acetate species were no longer detected, indicating that carbonate species were formed. These results indicate that Pt addition to the Ni catalyst promoted the oxidation and decomposition of ethoxy species. In fact, these experiments showed that the presence of Pt favored the ethanol/acetaldehyde decomposition reaction. When temperature was increased to 723 K, the intensity of the bands related to carbonate species decreased and the band typical of CO linearly adsorbed on Pt was vanished.

Comparison of the DRIFT spectra obtained following interaction of the reaction mixture with the PtNi/CeO$_2$ and Ni/CeO$_2$ catalysts provides evidence that addition of Pt promoted the formation of acetate species and its decomposition to methane and carbonate species. Moreover, comparison of the DRIFTS spectra of Pt/CeO$_2$, Ni/CeO$_2$ and PtNi/CeO$_2$ catalysts reveals marked differences. Both monometallic Ni and Pt catalysts promoted the decomposition of ethoxy species and/or oxidation of ethoxy species to acetate species. The Ni catalyst also favored the decomposition of acetate species and/or their oxidation to carbonate species, followed by decomposition to CO$_2$, whereas Pt catalyst improved ethanol decomposition even at very low temperatures. The bimetallic catalyst was found to combine these promotional effects.

Comparison of DRIFTS (Fig. 3) with transient-MS (Fig. 2) spectra provides evidence that the main reaction pathway for LTSR of ethanol over the studied catalysts is the decomposition of dehydro-
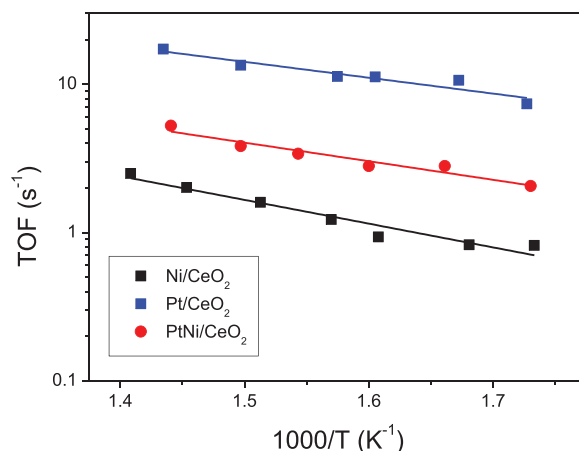

Fig. 4. Turnover frequency as a function of reaction temperature for Ni/CeO$_2$, Pt/CeO$_2$ and PtNi/CeO$_2$ catalysts.

genated (ethoxy, acetaldehyde, acetyl) and acetate species formed, to hydrogen, methane, CO and carbonate species.

3.3. Kinetic aspects of LTSR of ethanol

Specific catalytic activity of monometallic and bimetallic catalysts was determined in the form of TOFs, which are rates per exposed metal atom. No differentiation can be made in contributions of Ni and Pt surface atoms. Turnover frequencies of ethanol conversion were determined from experiments in which ethanol conversion was maintained below 10%, taking into account the dispersion of the catalysts (Table 1). Results are summarized in the Arrhenius-type diagram of Fig. 4. It seems that the intrinsic activity per exposed metal atom for the three catalysts studied follows the decreasing order Pt > PtNi > Ni. The higher activity of platinum for ethanol steam reforming has been reported by several authors [12,54,60–62]. The XPS results reported earlier suggest that Pt may have segregated on the outer surface of the Ni particles, thus participating directly in the reaction. Thus, the enhancement of TOF of the bimetallic catalyst, as compared to the Ni catalyst, may be due to the presence of the more active Pt particles on the Ni surface.

Ethanol conversion and product distributions as a function of time on stream (TOS) for SR of ethanol at 573 K over Pt/CeO$_2$, Ni/CeO$_2$ and PtNi/CeO$_2$ catalysts are shown in Fig. 5. For Pt/CeO$_2$ and Ni/CeO$_2$ catalysts, initial ethanol conversion was approximately 52 and 58%, respectively. The addition of Pt increased the initial ethanol conversion to 65%. H$_2$, CO, CH$_4$, CO$_2$, acetaldehyde and small amounts of acetone were observed for all catalysts. However, product distribution strongly varied depending on the catalyst. For Pt/CeO$_2$ and PtNi/CeO$_2$ catalysts, H$_2$, CO and CH$_4$ were the main products formed, indicating that ethanol decomposition is the main reaction taking place. On the other hand, the formation of CO and CH$_4$ significantly decreased for Ni/CeO$_2$ catalyst, suggesting that this reaction did not occur in a significant extent. In this case, the main products were H$_2$, CO$_2$ and acetaldehyde. The formation of H$_2$ and acetaldehyde indicates that ethanol dehydrogenation is favored. These results are in agreement with the transient and DRIFTS experiments that revealed Pt addition promoted the ethanol decomposition reaction. Taking into account the XPS experiments, these results might be attributed to the presence of a Pt overlayer.

Ethanol conversion decreased at the beginning of the SR reaction tests for all catalysts studied. However, the decrease in ethanol conversion was less significant for Pt/CeO$_2$ and PtNi/CeO$_2$ catalysts. In order to determine the main causes of catalyst deactivation, the
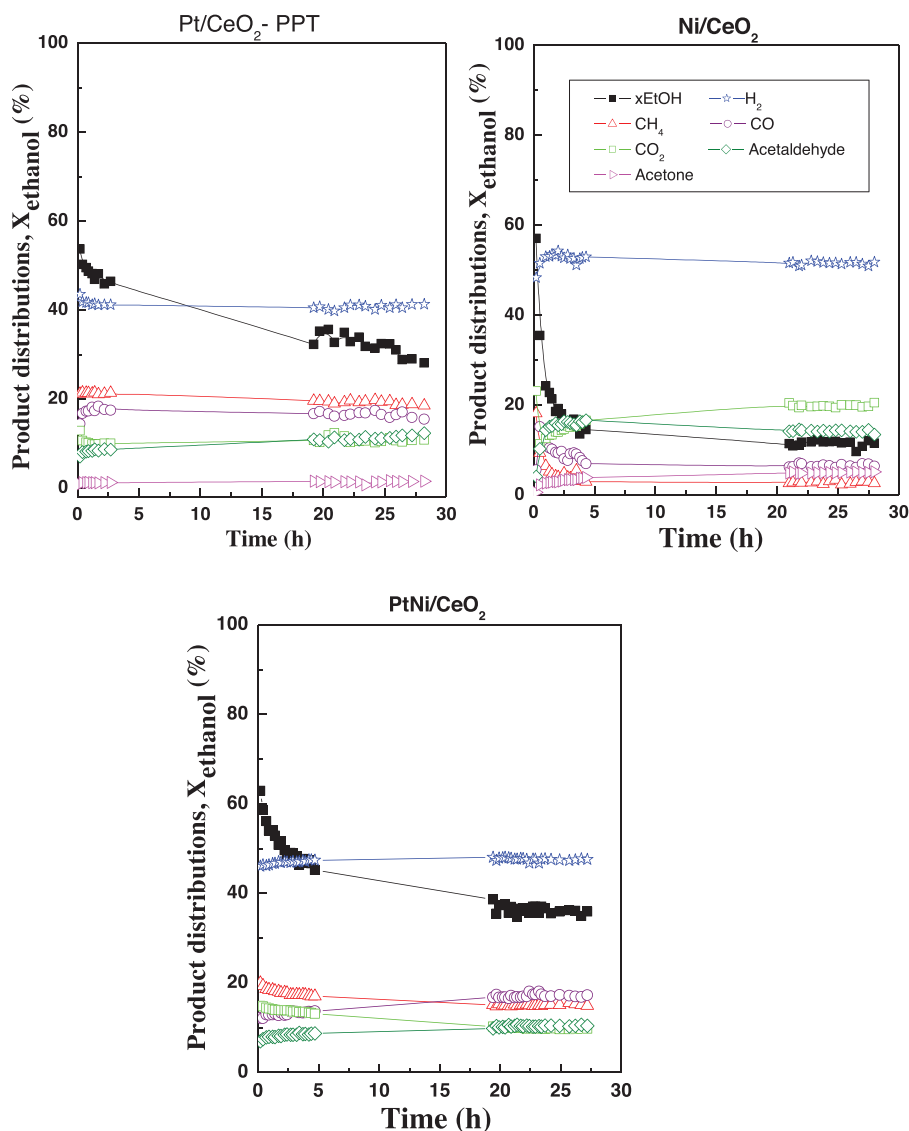
Fig. 5. Ethanol conversion ($X_{ethanol}$) and product distributions *versus* TOS for SR of ethanol at 573 K under H_2O/ethanol molar ratio = 3.0 over Pt/CeO_2, Ni/CeO_2 and $PtNi/CeO_2$. (Mass of catalyst = 100 mg and residence time = 0.1 g s/mL).

used catalysts were characterized by SEM and TG analysis and the results obtained are presented in the following section.

3.4. Characterization of post-reaction Ni supported catalysts

The SEM images of post-reaction Pt/CeO_2, Ni/CeO_2 and $PtNi/CeO_2$ catalysts (Fig. S3) did not show the presence of carbon filaments. The Raman spectra of the used Ni/CeO_2 and $PtNi/CeO_2$ catalysts shows the presence of two bands in the range between 1200 and 1700 cm^{-1}, which are associated with the D and G vibrational modes of carbon materials (Fig. S4). However, carbon was not detected on Pt/CeO_2 catalyst. The TPO profiles of Pt/CeO_2, Ni/CeO_2 and $PtNi/CeO_2$ catalysts after SR at 573 K for 28 h are presented in Fig. 6. The TPO profiles of Ni-based catalysts exhibited two peaks at 508–518 K and 702–722 K, whereas only one peak (507 K) is observed for Pt/CeO_2 catalyst. Some authors [63,64] studied the nature of the carbonaceous deposits and the amount of carbon deposited over supported Ni catalysts after SR of ethanol using TPO analyses. Fatsiskostas et al. [63] attributed the peak at low temperature (<530 K) to the decomposition of carbonates present on the surface. Augustin et al. [64] observed a broad peak between 673 and
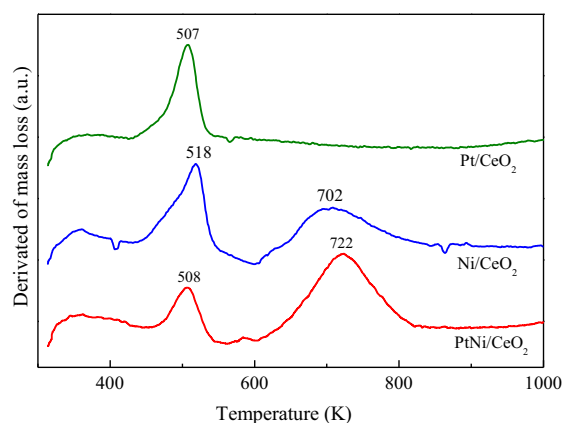

Fig. 6. TPO profiles of Pt/CeO_2, Ni/CeO_2 and $PtNi/CeO_2$ catalysts after SR of ethanol at 573 K for 28 h TOS.

873 K and a peak at around 859 K during TPO of different Ni catalysts supported on $ZnAl_2O_4$, after SR of ethanol at 773 K. The peak at low temperature was assigned to the oxidation of amorphous carbon
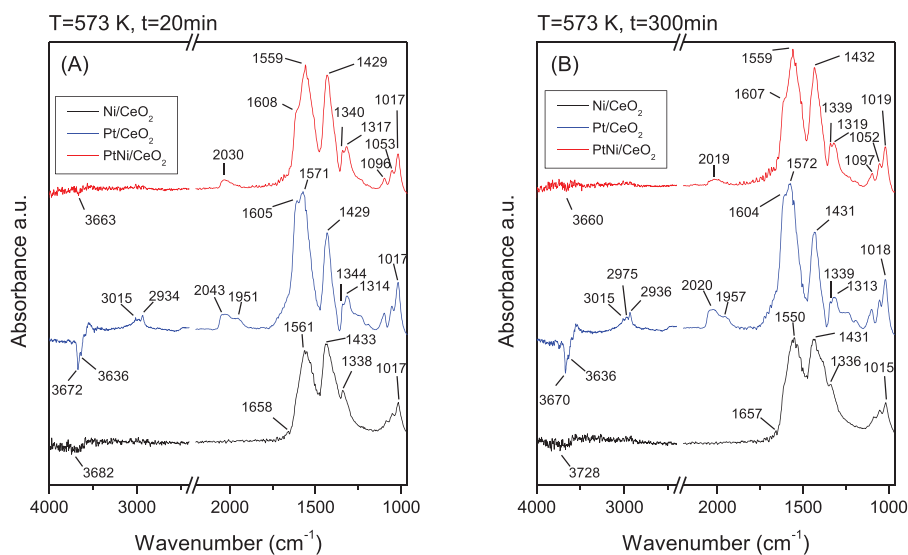
Fig. 7. DRIFT spectra obtained at 573 K over Ni/CeO$_2$, Pt/CeO$_2$ and PtNi/CeO$_2$ catalysts after (A) 20 min and (B) 300 min under the reaction mixture 0.5% ethanol, 1.5% water (He balance).
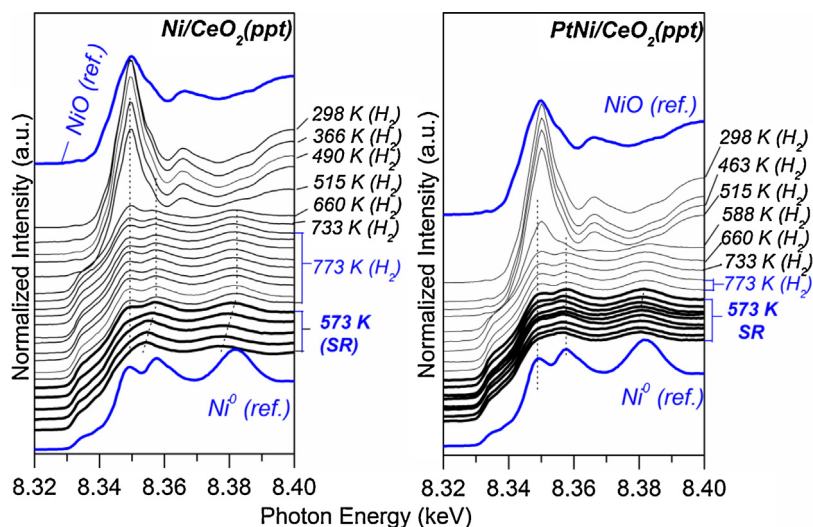

Fig. 8. *in-situ* XANES spectra of CeO$_2$ supported Ni and PtNi catalysts under different treatments.

overlaying the nickel surface, whereas the peak at high temperature was due to oxidation of filamentous carbon. Therefore, the two CO$_2$ peaks observed in our TPO could be attributed to the presence of two different types of carbon on the surface of the spent catalyst: carbonates and amorphous carbon. However, amorphous carbon was not detected on Pt/CeO$_2$ catalyst. The TG analysis did not reveal the formation of carbon filaments, which should be oxidized at higher temperatures. This result agrees very well with those obtained by SEM analyses. In addition, the DRIFTS experiments revealed that carbonate species are formed during reaction at 573 K and remain on the surface.

The amount of amorphous carbon deposited on Ni/CeO$_2$ and PtNi/CeO$_2$ catalysts after different reaction conditions, as determined by TG analysis, is listed in Table 4. Upon SR of ethanol at 573 K, the rate of formation of amorphous carbon per unit mass of catalyst (mgC/gcat/h) on PtNi/CeO$_2$ was slightly higher than that deposited on monometallic Ni catalyst. In comparison to the literature [18], these values were extremely low. Palma et al. [18] carried out an extensive review of the carbon formation rates reported in

Table 4

Amount of amorphous carbon deposited on Ni/CeO$_2$ and PtNi/CeO$_2$ catalysts after SR of ethanol at 573 K.

Sample	mgC/gcat/h	mgC/gcat/h/mole reacted ethanol
Ni/CeO$_2$	0.63	0.032
PtNi/CeO$_2$	0.83	0,013

the literature for SR of ethanol. The amount of carbon deposited on different catalysts and reaction conditions varied from 0.125 to 2733.4 mg$_C$/g$_{cat}$/h. In addition, most of these results were obtained for SR of ethanol at temperatures higher than 723 K. However, carbon deposition rates are significantly affected by the reaction temperature, steam-to-carbon ratios, ethanol concentration and space velocity. Therefore, any comparison has to take into account the reaction conditions used. However, it is important to stress that the number of papers about SR of ethanol containing data about the carbon deposition rate is very limited and this information is scarcer when we consider only the works about LTSR (573–623K). Only references [14,18,21,23,28] provided carbon deposits rate

data for LTSR of ethanol (Table S1). Rosseti et al. [21]studied the performance of Ni/SiO$_2$ and Ni/ZrO$_2$ catalysts for LTSR of ethanol (573 K). Raman spectroscopy, SEM and TEM revealed the presence of carbon filaments over Ni/ZrO$_2$ catalyst. The rate of carbon deposition calculated by TPO was 18.8mgC/gcat.h. However, carbon deposits were not detected for Ni/SiO$_2$ catalyst. These results were attributed to the support acid sites. LTSR of ethanol was performed over Ni supported on CeO$_2$ with different morphologies [23]. The carbon deposition rates varied depending on ceria morphology (0.23–1.05 mgC/gcat/h). Therefore, the amount of carbon formed in our work (Ni/CeO$_2$: 0.63 mgC/gcat/h; PtNi/CeO$_2$: 0.83 mgC/gcat/h) was quite low. However, any comparison concerning the amount of carbon formed between the two samples is somewhat hampered by the fact that the samples present rather different deactivation behavior. In order to take into account the strong deactivation of Ni/CeO$_2$ catalyst, the rate of deposition of amorphous carbon was calculated in mgC/gcat/h/mole of converted ethanol and the results are listed in Table 4. Although the addition of Pt has decreased the rate of deposition of amorphous carbon during reaction, the amount is still very low for both catalysts (Ni/CeO$_2$: 0.032 mgC/gcat/h/mole reacted ethanol; PtNi/CeO$_2$: 0013 mgC/gcat/h/mole reacted ethanol). Then, the significant deactivation observed on Ni/CeO$_2$ and PtNi/CeO$_2$ catalysts during reaction cannot be attributed only to the deposition of amorphous carbon.

Recently, DRIFTS spectra obtained during SR reaction under a steady flow of the ethanol + water mixture over Pt/CeO$_2$ [65] and Pt/CeZrO$_2$ [66] revealed that the intensities of bands assigned to acetate species increased with TOS, which was accompanied by a decrease in those corresponding to adsorbed CO over Pt. This result suggested that the rate of surface acetate decomposition decreased during reaction. It was proposed that the decrease in the intensity of the adsorbed CO band was attributed to a loss in Pt active sites due to the accumulation of CH$_x$ species at the Pt–support interface, resulting in catalyst deactivation.

In order to investigate the evolution of the intermediate species formed over the catalyst surface during reaction at 573K, DRIFTS spectra were recorded during 5 h under a steady flow of the ethanol + water mixture (Fig. 7). Comparing the results obtained with the spectra presented on Fig. 3, it is noticed the same characteristic bands at 573 K, indicating the presence of acetate and carbonate species. However, the relative intensities of those bands increased during 6 h of TOS and the increase was more important for Ni/CeO$_2$ catalyst. Therefore, these results show that there is accumulation of acetate or carbonate species on catalyst surface during reaction at low temperature (573 K) and their concentration remains high.
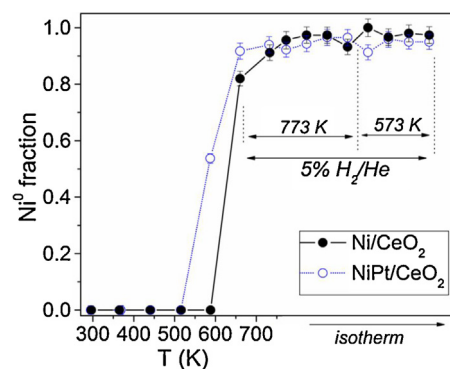

Fig. 9. LC-XANES of CeO$_2$ supported Ni and NiPt catalysts during reduction under 5% H$_2$/He flow.

3.5. XANES/EXAFS studies under reaction conditions

In situ XAS studies were performed in order to investigate the oxidation of metal particles [5,37,38]. The CeO$_2$ supported Ni and PtNi samples were examined by X-ray absorption at energies about the Ni K-edge (8.333 keV), in order to investigate potential changes in the structure of the metallic phase upon exposure to SR of ethanol conditions, after reduction under 5% H$_2$/He flow. Several EXAFS spectra were recorded, while temperature was varied according to a program that involved: (i) heating from 298 K to 773 K under H$_2$/He flow, (ii) keeping temperature at 773 K for 1 h under H$_2$/He flow, (iii) cooling to 573 K under H$_2$/He flow, (iv) SR of ethanol at 573K for 2 h. Consecutive spectra were recorded over the entire experiment.

Fig. 8 shows XANES spectra of Ni K-edge recorded from both CeO$_2$ supported Ni and PtNi catalysts. The decrease of the intensity of the white line in XANES spectra indicate the progressive reduction of NiO under 5% H$_2$/He mixture, as temperature was increased to 773 K. The spectra also revealed that Pt addition promoted the reduction of NiO at lower temperature.

Fig. 9 displays the evolution of the Ni species during reduction in a more quantitative basis by the linear combination of Ni K-edge XANES spectra of references. Although the final extent of reduction of both catalysts were similar after reduction at 773 K, the presence of Pt leads to its attainment at lower temperature, in accordance with the well know effect of Pt to promote the reduction of non noble metals oxides, as demonstrated by the TPR experiments.
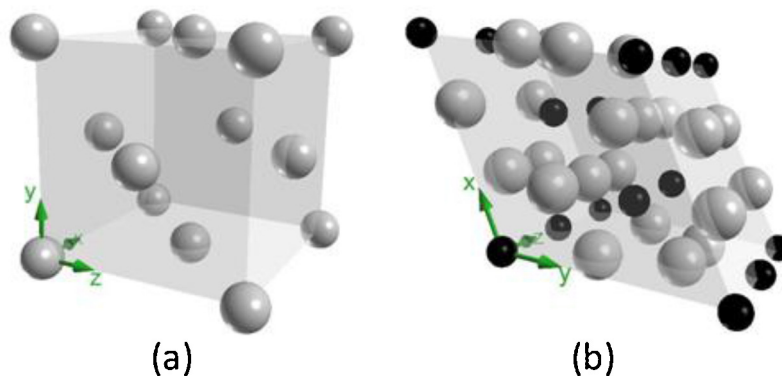

Fig. 10. CristalOgraph software package [http://escher.epfl.ch/crystalOgraph] built models for Ni fcc (a) and Ni$_3$C (hexagonal) considered in our EXAFS fittings. Nickel and carbon atoms are represented by gray and black spheres, respectively.

After 1 h reduction at 773 K under H_2/He flow, an EtOH:H_2O:He mixture was admitted into the reaction chamber at 573 K. The XANES spectra recorded at these conditions are shown in bold line in Fig. 8. The fine structure observed in the Ni K-edge XANES spectrum (three peaks located at 8.349, 8.358, 8.382 keV) underwent changes when the Ni/CeO$_2$ catalyst was treated under SR of ethanol conditions. In fact, after 2 h treatment, the three peaks gave rise to a two peaked fine structure (located at 8.377, 8.354 keV) that cannot be ascribed to either NiO or Ni^0 reference spectra (blue lined XANES spectra). Interestingly, only slight changes in the XANES spectra after 2 h under SR of ethanol are observed in the PtNi/CeO$_2$, indicating that Ni was mostly in the metallic phase after 2 h under SR of ethanol in the Pt promoted catalyst.

Comparison of the catalyst spectra with references spectra indicate that Ni is totally reduced to Ni^0 under H_2/He flow at 773 K, as spectra of the reduced catalysts are very similar to the one of Ni foil. Another observation is that even though the fine structure of XANES spectra considerably changes after exposure of Ni/CeO$_2$ to the SR of ethanol mixture, the spectra feature changes do not converge towards Ni^0 or NiO, which indicates that the formation of a new Ni containing phase takes place in the Ni/CeO$_2$ catalyst after 2 h exposure to SR of ethanol at 573 K. Considering that neither pure Ni^0 nor Ni^{2+} seem to be present in Ni/CeO$_2$ after 2 h treatment under reaction conditions, the more likely Ni containing phase that might be forming would be nickel carbides (NiC$_x$). Transition metal carbides may form where the metal is essentially zero-charged. In fact, those late transition metal carbides (e.g., FeC$_x$, CoC$_x$, NiC$_x$, etc.) may be thought as a solid solution in which carbon atoms occupy the octahedral sites of the metal lattice. Lattice distortions due to carbon induced metal–metal bond relaxation may take place, which in part explain the rather variable stoichiometries and structures found in those carbides. For instance, in the particular case of the NiC$_x$ system, NiC, Ni$_2$C and Ni$_3$C are the most stable phases. Ni$_3$C may assume either an orthorrombic or a hexagonal/rhombohedral structure, having the latter structure lower formation energy [67]. The structure and stoichiometry of those Ni carbides may vary with carburization temperatures [67,68]. For example, the product of the carburization of Ni powder with CO at 538 K was shown to be Ni$_3$C [69], whose relatively low formation energy allows its selective formation even at relatively low temperatures, such as 538 K. As a general mechanism, it has been pointed out that carbon may diffuse throughout the fcc lattice occupying its octahedral sites. That may lead to cell expansion which would decrease the potential barrier for even further carburization [70].

EXAFS fitting spectra of our samples reduced at 773 K, cooled to 573 K under H_2/He mixture, and then after 2 h under flow of ethanol:H_2O:He mixture at 573 K (this latter EXAFS spectrum recorded after cooling the sample down to room temperature under He flow) were also carried out. FEFF6 software package was used to build theoretical models for both Ni fcc and Ni$_3$C (based on reference [69]). The XRD-derived Ni$_3$C and Ni^0 crystallographic data used as inputs were JCPDS 06-0697 and JCPDS 04-0850, respectively, according to the work of Uhlig et al. [71]. Ni$_3$C is depicted as an arrangement of Ni atoms where each atom is surrounded by two carbon atoms located at 1.83 Å and by twelve Ni atoms located at distances around 2.63 Å. Those distances are considerably longer than those found in the Ni fcc unit cell (2.48 Å), which confirms that the presence of C somewhat relaxes the strong Ni–Ni interactions. The pictorial representations of Ni fcc and Ni$_3$C unit cell are shown in Fig. 10 [72].

First coordination shell fittings were performed in our spectra and the best fitting structural parameters are presented in Table 5A. The k^1-weighed k and r space EXAFS, along with their respective first coordination shell fits are displayed in Figs. 11 and 12. Both samples (Ni/CeO$_2$ and PtNi/CeO$_2$) reduced at 773 under dilute H_2 flow were well fitted using Ni fcc, which indicates that Ni is mostly
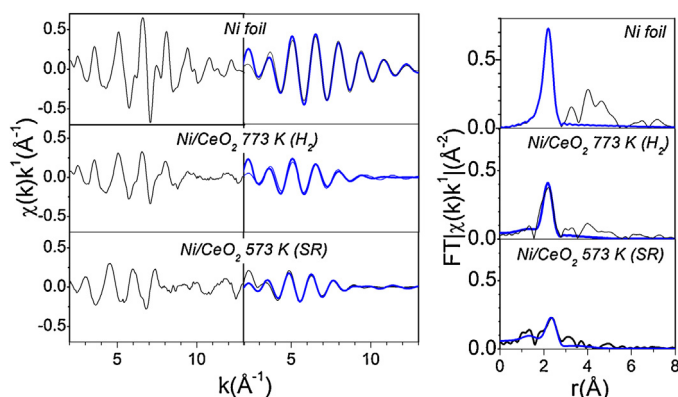

Fig. 11. Raw (left) and backtransformed (middle column) k-space Ni K-edge EXAFS spectra and Fourier-transformed, R space (right column) EXAFS spectra of Ni/CeO$_2$ after reduction under 5% H_2/He flow at 773 K (H_2) and after 2 h under SR of ethanol conditions (SR) (the spectrum was recorded at 298 K). First shell EXAFS fits are shown in blue lines. R-space spectra (k^1 weighed) are phase uncorrected. Transmission mode.
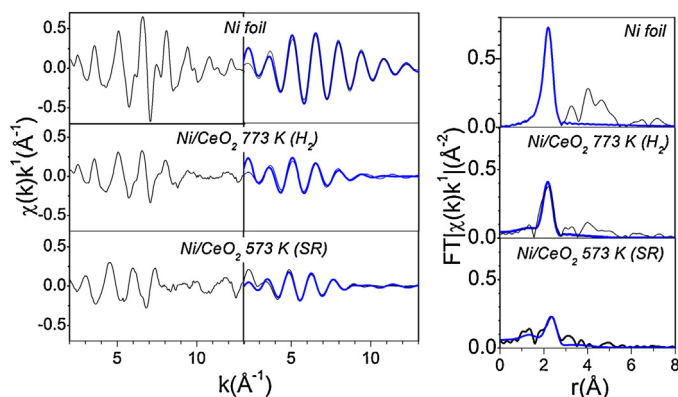

Fig. 12. Raw (left) and backtransformed (middle column) k-space Ni K-edge EXAFS spectra and Fourier-transformed, R space (right column) EXAFS spectra of PtNi/CeO$_2$ after reduction under 5% H_2/He flow at 773 K (H_2) and after 2 h under SR of ethanol conditions (SR) (the spectrum was recorded at 298 K). First shell EXAFS fits are shown in blue lines. R-space spectra (k^1 weighed) are phase uncorrected. Transmission mode.

in its metallic state upon reduction. However, EXAFS spectrum of Ni/CeO$_2$ catalyst after 2 h under SR of ethanol was best fitted by considering the presence of orthorhombic Ni$_3$C, along with Ni fcc. In fact, close examination of the k-spaced EXAFS allows one to see that Ni/CeO$_2$ presents a phase shift toward lower k that is not observed on PtNi/CeO$_2$. The observed downward shift qualitatively indicates that a further atom is placed at a closer distance to Ni, on Ni/CeO$_2$ after 2 h of SR of ethanol. This does not seem to occur at the same extent on PtNi/CeO$_2$ exposed to the same conditions. In fact, a mixed model considering both Ni fcc and Ni$_3$C could be used to fit PtNi/CeO$_2$ EXAFS spectra, as well.

Fig. 13 shows the Fourier Transformed EXAFS spectra (FT-EXAFS) of both Ni/CeO$_2$ (Fig. 13A) and PtNi/CeO$_2$ (Fig. 13B) under different conditions: (i) after 1 h reduction at 773 K and cooling to 573 K, still under 5%H_2/He flow (thin, dark line); (ii) after 2 h of reaction at 573 K (blue line) and (iii) after cooling the reactor to 298 K under He flow (red dotted line). The spectrum of Ni foil (thin dotted line) displays the distribution of atoms at distances referred to the first four coordination shells at distances below 6 Å from the absorber. Catalyst reduction at 773 K yields a spectrum that resembles Ni fcc in the first shell, with some distortions in farther shells probably due to temperature. For Ni/CeO$_2$, after two hours of reaction, the presence of a NiC$_x$ phase is evidenced by (i) the appearance of a structure below 2 Å indicating the presence of another scatterer,

Table 5

Best fit EXAFS Pt-L_{III} and Ni-K edge spectra for the PtNi/CeO$_2$ catalysts under either reducing or low temperature SR of ethanol conditions (as indicated in the table). Fits were made in the R-space, k^1 and k^2 weighed for the Ni and Pt edge spectra, respectively. Amplitude factor (S_0) were estimated to be 0.91 and 0.76 for Pt and Ni, respectively, by constraining N equal to 12, while floating the other variables in the metal foil spectra.

A) Transmission mode (S_0 (Ni) = 0.76)									
Samples	Conditions	Model	$R (10^{-3} Å)$	N	$\sigma^2 (10^{-3} Å^2)$	e_o (eV)	r(%)	Δr	Δk
Ni foil	RT	Ni fcc	**Ni–Ni^{fcc}: 2.4874 ± 0.0003**	12*	6.0 ± 0.1	5.9 ± 0.1	0.01	1.8-2.8	2.5-14
Ni/CeO$_2$	773 K/H$_2$	Ni fcc	**Ni–Ni^{fcc}: 2.48 ± 0.01** **Ni–C^{Ni3C}: 1.87 ± 0.04**	**Ni–Ni^{fcc}: 13 ± 2** **Ni–C^{Ni3C}: 1.7 ± 0.7**	18 ± 2	5.5 ± 0.9	1	1.8-2.8	2.5-12
	573 K/SR	Ni$_3$C+Ni fcc	**Ni–Ni^{Ni3C}: 2.64 ± 0.04** **Ni–Ni^{fcc}: 2.49 ± 0.04**	**Ni–Ni^{Ni3C}: 2.5 ± 1.3** **Ni–Ni^{fcc}: 5 ± 2**	11 ± 5	8 ± 1	4	1.5-2.8	2-12
PtNi/CeO$_2$	773 K/H$_2$	Ni fcc	**Ni–Ni^{fcc}: 2.475 ± 0.004** **Ni–Ni^{fcc}: 2.48 ± 0.03**	**Ni–Ni^{fcc}: 9 ± 1** **Ni–C^{Ni3C}: 0.7 ± 0.3**	12 ± 1	5.7 ± 0.8	0.9	1.8-2.8	2-12
	573 K/SR	Ni fcc+Ni$_3$C	**Ni–C^{Ni3C}: 1.85 ± 0.03** **Ni–Ni^{Ni3C}: 2.61 ± 0.03**	**Ni–Ni^{Ni3C}: 1.3 ± 0.6** **Ni–Ni^{fcc}: 6 ± 2**	8 ± 4	7 ± 1	5	1.0-2.7	1.5-12

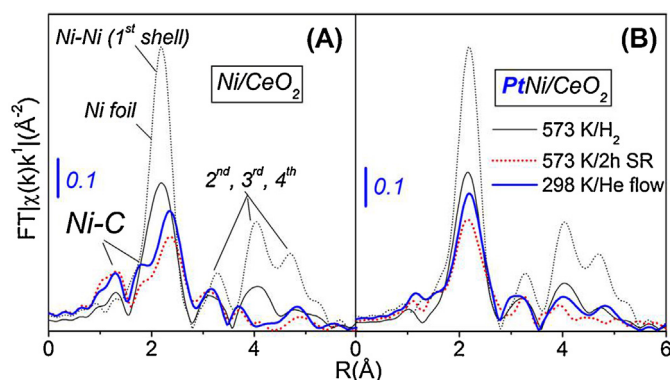| B) Fluorescence mode (S_0 (Ni) = 0.76; S_0 (Pt) 0.91). All spectra were recorded at 298 K.									
Samples	Conditions	Model	$R (10^{-3} Å)$	N	$\sigma^2 (10^{-3} Å^2)$	e_o (eV)	r(%)	Δr	Δk
Pt foil	298 K	Pt fcc	**Pt–Pt: 2.8 ± 0.5**	**Pt–Pt: 12***	5.0 ± 0.1	7.8 ± 0.5	0.2	2.0–3.5	3–15
PtNi/CeO$_2$	773 K/H$_2$	Pt fcc + Ni$_3$Ptfcc	**Pt–Ni: 2.630 ± 0.007** **Pt–Pt: 2.673 ± 0.007**	**Pt–Ni: 4.7 ± 1.5** **Pt–Pt: 1.5 ± 1.1**	7 ± 2	5 ± 3	3	2.0–3.5	2.5–12
	573 K/SR	Pt fcc + Ni$_3$Ptfcc	**Pt–Ni: 2.537 ± 0.007** **Pt–Pt: 2.661 ± 0.007**	**Pt–Ni: 2.7 ± 0.7** **Pt–Pt: 1.2 ± 0.3**	4 ± 2	6 ± 2		2.0–3.5	2.5–12
Ni foil	298 K	Ni fcc	**Ni–Ni^{fcc}: 2.482 ± 0.002**	**Ni–Ni: 12**	4.8 ± 0.6	6.6 ± 0.6	0.3	1.8–2.5	2.5–14
PtNi/CeO$_2$	773 K/H$_2$	Ni fcc	**Ni–Ni^{fcc}: 2.482 ± 0.001** **Ni–C^{Ni3C}: 1.84 ± 0.01**	**Ni–Ni: 10.4 ± 0.5** **Ni–C: 1.3 ± 0.4**	4.5 ± 0.4	6.5 ± 0.4	0.1	1.8–2.5	2.5–14
	573 K/SR	Ni fcc + Ni$_3$C	**Ni–Ni^{Ni3C}: 2.62 ± 0.01** **Ni–Ni^{fcc}: 2.48 ± 0.01**	**Ni–C–Ni: 1.6 ± 0.3** **Ni–Ni (fcc): 6.5 ± 1.2**	5 ± 2	6 ± 1	1	1.5–2.7	2–14

Fig. 13. k^1 weighed Fourier-transformed EXAFS spectra of Ni/CeO$_2$ (A) and PtNi/CeO$_2$ (B) after reduction under 5% H$_2$/He flow at 773 K for 1 h and cooled to 573 K (black line, spectra were recorded at 573 K), and after 2 h under SR of ethanol conditions (red dotted line) and after cooling the sample down to room temperature under He flow (blue line); in comparison to a spectrum from a Ni-foil reference (black dotted line). Phase uncorrected. (For interpretation of the references to color in this figure legend, the reader is referred to the web version of this article.)

(ii) the shift of the Ni–Ni peak to somewhat longer distances and (iii) the disruption of the peak pattern observed in the reference spectrum above 3 Å. Conversely, none of those changes are observed in PtNi/CeO$_2$, except the appearance of a small shoulder located below 2 Å, which indicate the presence of only residual amounts of nickel carbide.

Carbidic phases formed upon low temperature carburization of Ni (T < 773 K), particularly Ni$_3$C have been shown to be the precursors for the formation of Ni-catalyzed carbon nanostructures [73–75]. The mechanisms of carbon formation and the growth of filaments for steam reforming and the decomposition of methane over supported Ni catalysts are well-described [76–80]. Methane dissociates on the nickel surface, and this produces highly reactive carbon species (Cα) [79]. This carbon may react with water and then it is removed from the surface. However, if the gasification rate is low, Cα formed may undergo polymerization to less active carbon (Cβ). As a result, it may accumulate on the surface or may dissolve in the nickel lattice. According to Trimm [79,80],

nickel carbide is considered an intermediate in the carbon dissolution process. The dissolution of carbon into the Ni crystallite leads to the nucleation and growth of carbon filaments (e.g., whiskers). Then, the nickel carbide can be considered as an important intermediate in the mechanism of carbon formation. [79,80]. In that sense, inhibiting carbide formation has been proposed as an approach for minimizing carbon formation [80].

The formation of Ni carbides has also been reported in the literature as the responsible for catalyst deactivation during SR of ethanol. A Ni/ZnAl$_2$O$_4$ catalyst deactivated during SR of ethanol at 773 K [64]. The diffractogram of the used catalyst revealed the presence of metallic Ni phase, nickel carbide (Ni$_3$ZnC$_{0.7}$) and graphitic carbon. Fierro et al. [81] compared the long term stability of Ni/SiO$_2$ and Ni-Cu/SiO$_2$ catalysts for OSR of ethanol. The monometallic catalyst significantly deactivated during TOS. The selectivity to H$_2$ decreased whereas the selectivity to acetaldehyde and ethylene as well as the formation of carbon increased. The bimetallic catalyst remained quite stable. The authors suggested that the addition of Cu inhibited the formation of Ni carbide.

PtNi/CeO$_2$ catalyst was probed by recording fluorescence mode EXAFS spectra in both Pt L$_{III}$ edge and Ni K-edge on the PtNi/CeO$_2$ sample, in a further attempt to investigate the role of Pt in the stabilization of the catalyst. The same pretreatments (1 h reduction at 773 K under H$_2$/He, 1 h reaction at 573 K under 1:1 ethanol:water mixture) as previously described were used here, with the difference that all EXAFS spectra were recorded at room temperature, for a better signal. Figs. 14 and 15 display the χ(k) (raw and back-transformed as a comparison to the fit) and Fourier transformed signals of both Pt (k^3 weighed) and Ni (k^1 weighed) edges and the fits obtained are reported in Table 5B. The occurrence of the first coordination shell peak at shorter distances than the Pt–Pt clearly indicates the presence of Ni on the first coordination shell of Pt. EXAFS spectra were modeled by considering scattering paths between Pt–Pt (in Pt fcc) and Pt-Ni (in a PtNi$_3$ fcc) bonds. Based on these results, it is suggested that Pt is mainly present as quite small PtNi$_3$ clusters, with some minor occurrence of Pt–Pt, in the catalyst reduced at 773 K. Comparing the EXAFS spectra on both edges, a model that better represents the PtNi system consists of bimetallic particles, with Pt mostly distributed over the Ni particle,
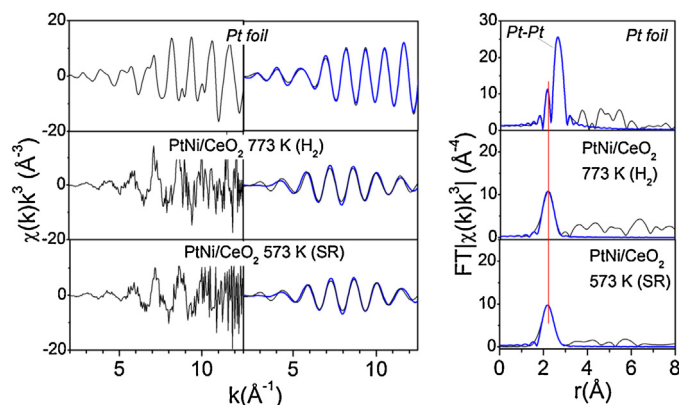
Fig. 14. Raw (left) and backtransformed (middle column) k-space Pt L_{III}–edge EXAFS spectra and Fourier-transformed, R space (right column) EXAFS spectra of PtNi/CeO$_2$ after reduction under 5% H$_2$/He flow at 773 K (H$_2$) and after 2 h under SR of ethanol conditions (SR). First shell EXAFS fits are shown in blue lines. R-space spectra (k^1 weighed) are phase uncorrected. Spectra recorded at 298 K, under fluorescence mode.
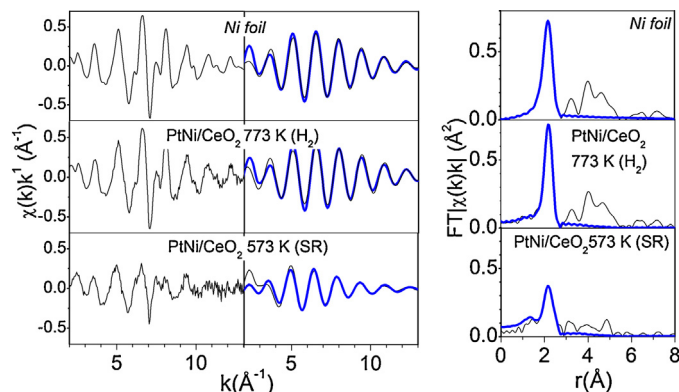

Fig. 15. Raw (left) and backtransformed (middle column) k-space Ni K-edge EXAFS spectra and Fourier-transformed, R space (right column) EXAFS spectra of PtNi/CeO$_2$ after reduction under 5% H$_2$/He flow at 773 K (H$_2$) and after 2 h under SR of ethanol conditions (SR). First shell EXAFS fits are shown in blue lines. R-space spectra (k^1 weighed) are phase uncorrected. Spectra recorded at 298 K, under fluorescence mode.

Fig. 16. Model depicting the dynamic transformations of the Ni containing phase upon activation and steam reforming of ethanol for both Ni/CeO$_2$ and NiPt/CeO$_2$ catalysts.

with a surface enrichment in the noble metal, and isolated Ni particles. This model agrees very well with TPR and XPS results. It should also be emphasized that the fact that the parameters obtained from the EXAFS fitting results of the PtNi/CeO$_2$ catalyst after reduction or reaction at the Ni K-edge (fluorescence vis-à-vis transmission modes) are similar, which reinforces the validity of the models used to fit those spectra.

Considering the above mentioned results, an explanation about why Ni/CeO$_2$ deactivated to a higher extent than PtNi/CeO$_2$ may be provided. The DRIFTS and transient experiments under reaction condition of both catalysts showed that the ethoxy species, the dehydrogenated species (acetaldehyde, acetyl species), and the acetate species can all decompose to H$_2$, CO, and CH$_x$. According to the reaction mechanism proposed for the SR of ethanol [5], the CH$_x$ species can be hydrogenated and desorbs as methane or may react with water producing H$_2$ and CO. Alternatively, this CH$_x$ species may be further dehydrogenated to carbon. Therefore, when the rate of this reaction pathway is higher than the rate of desorption of CH$_x$ species as CH$_4$, carbon is accumulated over the surface and the catalyst deactivates. In the case of Ni/CeO$_2$ catalyst, this carbon migrates through the Ni crystallite producing nickel carbide. For the PtNi/CeO$_2$ catalyst, the transient experiments revealed that methane was formed at a larger extent. In this case, the presence of Pt reduces catalyst deactivation likely by either increasing the
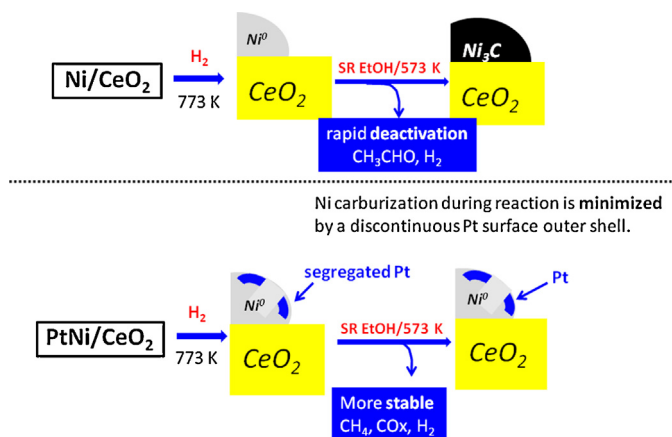
hydrogenation rate of CH$_x$ species or the reaction rate with water and, consequently minimizing nickel carbide formation. The role of Pt is to produce reactive hydrogen species by dissociative adsorption of hydrogen and spillover of adsorbed hydrogen atoms to the Ni surface. These highly reactive hydrogen atoms hydrogenate the adsorbed carbon precursor species, which eventually desorbs as methane. This step reduces the rate of formation of carbon on the surface of Ni and, thus, the rate of dissolution of carbon into the Ni matrix. A scheme of this model for both catalysts is suggested in Fig. 16.

Sanchez-Sanchez et al. [19] carried out DRIFTS experiments under ED and SR of ethanol at 673 K over Ni/Al$_2$O$_3$ and PtNi/Al$_2$O$_3$ catalysts. They proposed that the improved stability of the bimetallic catalyst is due to the enhanced ability of Pt to gasify the methyl groups formed as a result of the decomposition of the acetate species. In the case of the monometallic catalysts, these methyl groups are dehydrogenated to carbon.

Ni alloying with a noble metal may occur [82], as well, and that has been related to carbide inhibition [80,81]. However, in our work, XPS and EXAFS experiments did not provide any evidence for the formation of a PtNi alloy.

We have made a TPO of bulk Ni$_3$C under the same conditions the spent catalysts were studied. The TPO profile (not shown here) indicated a maximum weight gain in the sample (corresponding to the formation of the NiO) at c.a. 800 K. Considering that the amount of NiC$_x$ formed should be small, that region was totally overshadowed by the mass loss peak due to the oxidation of C out of the sample.

Finally, the causes of deactivation of Pt/CeO$_2$ catalyst still remain open. This could be due to Pt or ceria sintering during reaction. In order to check these possibilities, the CO hydrogenation reaction was carried out over Pt/CeO$_2$ catalysts before and after SR of ethanol reaction, considering that this is a structure insensitive reaction [83]. The same CO conversion (7%) and product distribution were obtained on both fresh and used catalysts. This result indicates that Pt sintering can be ruled out during the reaction. Moreover, the ceria crystallite size calculated before and after SR of ethanol reaction only slightly increased from 8.7 to 10.2 nm, revealing that ceria sintering was not significant. However, a high concentration of carbonate species was observed in the DRIFTS experiments under steady flow conditions at 573 K. This result is in agreement with TPO experiment that revealed the decomposition of carbonate species over all catalysts. Theses carbonate species present on the surface of the support during SR of ethanol may block the metal-support interface, leading to a decrease of ethanol conversion and catalyst deactivation.

4. Conclusions

In this paper, the effect of Pt addition on the performance of Ni/CeO$_2$ catalyst for the low temperature steam reforming of ethanol has been investigated. The *in situ* experiments allowed to correlate the structural modifications of the catalysts with their performance for the steam reforming of ethanol, which has not been previously reported in the literature for this reaction. The combination of our catalyst characterization data suggest that Pt may segregated toward the surface of the Ni particles and promoted the hydrogenation of highly active carbon species adsorbed at the surface at a higher rate than carbon diffusion into bulk nickel. Therefore, the formation of nickel carbide phase and amorphous carbon was minimized and consequently decreased catalyst deactivation of Ni-based catalysts. DRIFTS experiments also revealed the accumulation of carbonate species on the surface of the support during SR of ethanol, which may block the metal-support interface. This was the main cause of deactivation of Pt/CeO$_2$ catalyst.

Acknowledgements

Appendix A. Supplementary data

Supplementary data associated with this article can be found, in the online version, at 10.1016/j.apcatb.2015.08.04410.1016/j.apcatb.2015.08.044.

References

[1] A. Haryanto, S. Fernando, N. Murali, S. Adhikari, Energy Fuels 19 (2005) 2098.
[2] P.D. Vaidya, A.E. Rodrigues, Chem. Eng. J. 117 (2006) 39.
[3] M. Ni, Y.C. Leung, M.K.H. Leung, Int. J. Hydrogen Energy 32 (2007) 3238.
[4] P.R. de la Piscina, N. Homs, Chem. Soc. Rev. 37 (2008) 2459.
[5] L.V. Mattos, G. Jacobs, B.H. Davis, F.B. Noronha, Chem. Rev. 112 (2012) 4094.
[6] T. Hou, S. Zhang, Y. Chen, D. Wang, W. Cai, Renew. Sustain. Energy Rev. 44 (2015) 132.
[7] J.L. Contreras, J. Salmanes, J.A. Colin-Luna, L. Luno, B. Quintana, I. Cordova, B. Zeifert, C. Tapia, G.A. Fuentes, Int. J. Hydrogen Energy 39 (2014) 18835.
[8] A.F. Ghenciu, Curr. Opin. Solid State Mater. Sci. 6 (2002) 389.
[9] P. Panagiotopoulou, D.I. Kondarides, J. Catal. 225 (2004) 327.
[10] P. Panagiotopoulou, D.I. Kondarides, X.E. Verykios, Appl. Catal. B 88 (2009) 470.
[11] P. Panagiotopoulou, D.I. Kondarides, X.E. Verykios, Ind. Eng. Chem. Res. 50 (2011) 523.
[12] A.C. Basagiannis, P. Panagiotopoulou, X.E. Verykios, Top. Catal. 51 (2008) 2.
[13] P. Ciambelli, V. Palma, A. Ruggiero, Appl. Catal. B 96 (2010) 18.
[14] P. Ciambelli, V. Palma, A. Ruggiero, G. Iaquaniello, Appl. Catal. B 96 (2010) 190.
[15] J.A. Torres, J. Llorca, A. Casanovas, M. Domínguez, J. Salvadó, D. Montané, J. Power Sources 169 (2007) 158.
[16] B. Zhang, X. Tang, Y. Li, Y. Xu, W. Shen, Int. J. Hydrogen Energy 32 (2007) 2367.
[17] A.C.W. Koh, L. Chen, W.K. Leong, T.P. Ang, B.F.G. Johnson, T. Khimyak, J. Lin, Int. J. Hydrogen Energy 34 (2009) 5691.
[18] V. Palma, F. Castaldo, P. Ciambeli, G. Iaquaniello, Appl. Catal. B 145 (2014) 73.
[19] M.C. Sanchez-Sanchez, R.M.N. Yerga, D.I. Kondarides, X.E. Verykios, J.L.G. Fierro, J. Phys. Chem. A 114 (2010) 3873.
[20] X. Han, Y. Yu, H. He, J. Zhao, J Energy Chem 22 (2013) 861.
[21] I. Rosseti, J. Lasso, V. Nichele, M. Signoretto, E. Finocchio, G. Ramis, A. di Michele, Appl. Catal. B 150 (2014) 257.
[22] R. Trane-Restrup, S. Dahl, A.D. Jensen, Int. J. Hydrogen Energy 38 (2013) 15105.
[23] T.S. Moraes, R.C.R. Neto, M.C. Ribeiro, L.V. Mattos, M. Kourtelesis, X. Verykios, F.B. Noronha, Topics Catal. 58 (2015) 281.
[24] E. Moretti, L. Stonaro, A. Talon, S. Chitsazan, G. Garbarino, G. Busca, E. Finocchio, Fuel 153 (2015) 166.
[25] Y. Sekine, Y. Nakazawa, K. Oyama, T. Shimizu, S. Ogo, Appl. Catal. B 472 (2014) 113.
[26] L.C. Chen, S.D. Lin, Appl. Catal. B 148 (2014) 509.
[27] V. Palma, F. Castaldo, P. Ciambelli, G. Iaquaniello, G. Capitani, Int. J. Hydrogen Energy 38 (2013) 6633.
[28] L. Zhang, W. Li, J. Liu, C. Guo, Y. Wang, J. Zhang, Fuel 88 (2009) 511.
[29] G.P. Szijjarto, Z. Paszti, I. Sajo, A. Erdohelyi, G. Radnoczi, A. Tompos, J. Catal. 305 (2013) 290.
[30] J.Y.Z. Chiou, W.Y. Wang, S.Y. Yang, C.L. Lai, H.H. Huang, C.B. Wang, Catal. Lett. 143 (2013) 501.
[31] F. Soyal-Baltacioglu, A.E. Aksoylu, Z.I. Onsan, Catal. Today 138 (2008) 183.
[32] V. Palma, E. Palo, F. Castaldo, P. Ciambeli, G. Iaquaniello, Chem. Eng. Trans. 25 (2011) 947.
[33] V. Palma, E. Palo, F. Castaldo, P. Ciambeli, G. Iaquaniello, Chem. Eng. Trans. 29 (2012) 109.
[34] P. Panagiotopoulou, D.I. Kondarides, Catal. Today 112 (2006) 49.
[35] P. Panagiotopoulou, D.I. Kondarides, Catal. Today 127 (2007) 319.
[36] P. Ciambelli, V. Palma, A. Ruggiero, G. Iaquaniello, Chem. Eng. Trans. 17 (2009) 19.
[37] C.N. Ávila-Neto, J.W.C. Liberatori, A.M. da Silva, D. Zanchet, C.E. Hori, F.B. Noronha, J.M.C. Bueno, J. Catal. 287 (2012) 124.
[38] E.B. Pereira, N. Homs, S. Marti, J.L.G. Fierro, P.R.J. de la Piscina, J. Catal. 257 (2008) 206.
[39] T.S. Moraes, R.C.R. Neto, M.C. Ribeiro, L.V. Mattos, M. Kourtelesis, S. Ladas, X. Verykios, F.B. Noronha, Catal. Today 242 (2015) 35.
[40] J.J. Yeh, I. Lindau, At. Data Nucl. Data Tables 32 (1985) (2011) 1–155.
[41] M. Newville, J. Synchrotron Rad. 8 (2001) 96.
[42] T. Chafik, D.I. Kondarides, X.E. Verykios, J. Catal. 190 (2000) 446.
[43] A.C. Basagiannis, X.E. Verykios, Appl. Catal. A 308 (2006) 182–193.
[44] F.B. Passos, E.R. de Oliveira, L.V. Mattos, F.B. Noronha, Catal. Today 101 (2005) 23.
[45] J.L. Ewbank, L. Kovarik, F.Z. Diallo, C. Sievers, Appl. Catal. A: General 494 (2015) 57–67.
[46] E. Beche, P. Charvin, D. Perarnau, S. Abanades, G. Flamant, Surf. Interf. Anal. 40 (2008) 264.
[47] B. Luo, S. Xu, Y. Yan, Q. Xue, J. Electrochem. Soc. 160 (2013) 262–268.
[48] M.P. Anderson, T. Bligaard, A. Kustov, K.E. Larsen, J. Greeley, T. Johannessen, C.H. Christensen, J.K. Nørskov, J. Catal. 239 (2006) 501.
[49] R.E. Hayes, W.J. Thomas, K.E. Hayes, J. Catal. 92 (1985) 312.
[50] V.L. Kuznetsov, S.P. Noskova, I.L. Kuznetsova, Yu I. Yermakov, React. Kinet. Catal. Lett. 38 (1989) 411–416.
[51] H. Idriss, C. Diagne, J.P. Hindermann, A. Kiennemann, M.A. Barteau, J. Catal. 155 (1995) 219.
[52] A. Yee, S.J. Morrison, H. Idriss, J. Catal. 186 (1999) 279.
[53] S.M. Lima, I.O. da Cruz, G. Jacobs, B.H. Davis, L.V. Mattos, F.B. Noronha, J. Catal. 257 (2008) 356.
[54] A. Yee, S.J. Morrison, H. Idriss, Catal. Today 63 (2000) 327.
[55] A.M. da Silva, K.R. de Souza, G. Jacobs, U.M. Graham, B.H. Davis, L.V. Mattos, F.B. Noronha, Appl. Catal. B 102 (2011) 94.
[56] A. Erdohelyi, J. Rasko, T. Kecskes, M. Toth, M. Domok, K. Baan, Catal. Today 116 (2006) 367.
[57] G. Jacobs, R.A. Keogh, B.H. Davis, J. Catal. 245 (2007) 326.
[58] J. Raskó, A. Hancz, A. Erdőhelyi, Appl. Catal. A: Gen. 269 (2004) 13.
[59] P.V. Menacherry, G.L. Haller, J. Catal. 177 (1998) 175.
[60] F. Aupretre, C. Descorme, D. Duprez, Catal. Commun. 3 (2002) 263.
[61] J.P. Breen, R. Burch, M. Coleman, Appl. Catal. B: Environ. 39 (2002) 65.
[62] J. Sun, X.P. Qiu, F. Wu, W.T. Zhu, Int. J. Hydrogen Energy 30 (2005) 437–445.
[63] A.N. Fatsikostas, X.E. Verykios, J. Catal. 225 (2004) 439.
[64] E. Agustín, E. Galetti, M.F. Gomez, L.A. Arrua, M.C. Abello, Appl. Catal. A 348 (2008) 94.
[65] S.M. Lima, A.M. Silva, G. Jacobs, B.H. Davis, L.V. Mattos, F.B. Noronha, Appl. Catal. B 96 (2010) 387.
[66] S.M. Lima, A.M. Silva, U.M. Graham, G. Jacobs, B.H. Davis, L.V. Mattos, F.B. Noronha, Appl. Catal. A 352 (2009) 95.
[67] J.S. Gibson, J. Uddin, T.R. Cundari, N.K. Bodiford, A.K. Wilson, J. Phys. Condens. Matter 22 (2010) 44503.
[68] M. Akiyama, Y. Oki, M. Nagai, Catal. Today 181 (2012) 4.
[69] R.P.W.J. Struis, D. Bachelin, C. Ludwig, A. Wokaun, J. Phys. Chem. C 113 (2009) 2443.
[70] J. Xu, M. Saeys, J. Phys. Chem. C 112 (2008) 9679.
[71] S. Uhlig, R. Struis, H.S. Engel, J. Bock, A.C. Probst, O.F. Weber, I. Zizak, R. Chernikov, G. Schultes, Diam. Rel. Mat. 34 (2013) 25.
[72] G. Chapuis, N. Schoeni, CrystalOgraph, an interactive applet for drawing crystal structures. École Polytechnique Fédérale de Lausanne http://escher. epfl.ch/crystalOgraph.
[73] G. Odahara, S. Otani, C. Oshima, M. Suzuki, T. Yasue, T. Koshikawa, Surf. Sci. 605 (2011) 1095.
[74] L.L. Patera, C. Africh, R.S. Weatherup, R. Blume, S. Bhardwaj, C. Castellarin-Cudia, A. Knop-Gericke, R. Schlögl, G. Comelli, S. Hofmann, C. Cepek, Nano 7 (2013) 7901.
[75] J. Lahiri, T. Miller, L. Adamska, I.I. Oleynik, M. Batzill, Nano Lett. 11 (2011) 518.
[76] J.R. Rostrup-Nielsen, Catal. Today 18 (1993) 305.
[77] J.R. Rostrup-Nielsen, T. Rostrup-Nielsen, CATTECH 6 (2002) 150.
[78] J.R. Rostrup-Nielsen, J. Sehested, J. Norskov, Adv. Catal. 47 (2002) 65.
[79] D.L. Trimm, Catal. Today 37 (1997) 233.
[80] D.L. Trimm, Catal. Today 49 (1999) 3.
[81] V. Fierro, O. Akdim, C. Mirodatos, Green Chem. 5 (2003) 20.
[82] G. Jacobs, W. Ma, P. Gao, B. Todic, T. Bhatelia, D.B. Bukur, B.H. Davis, Catal. Today 214 (2013) 100.
[83] G.A. Somorjai, Introduction to Surface Chemistry and Catalysis, Wiley, 2010.